ISTANBUL TECHNICAL UNIVERSITY ★ INFORMATICS INSTITUTE

NONLINEAR IMAGING OF DIELECTRIC OBJECTS
BURIED UNDER A ROUGH SURFACE

Ph.D. THESIS

Tolga Ulaş GÜRBÜZ

Department of Communication Systems

Satellite Communication and Remote Sensing Programme

JANUARY 2014

ISTANBUL TECHNICAL UNIVERSITY ★ INFORMATICS INSTITUTE

NONLINEAR IMAGING OF DIELECTRIC OBJECTS
BURIED UNDER A ROUGH SURFACE

Ph.D. THESIS

Tolga Ulaş GÜRBÜZ
(705072006)

Department of Communication Systems

Satellite Communication and Remote Sensing Programme

Thesis Advisor: Prof. Dr. Ibrahim AKDUMAN

JANUARY 2014

İSTANBUL TEKNİK ÜNİVERSİTESİ ★ BİLİŞİM ENSTİTÜSÜ

ENGEBELİ YÜZEYLER ALTINA GÖMÜLÜ DİELEKTRİK CİSİMLERİN DOĞRUSAL OLMAYAN YÖNTEMLERLE GÖRÜNTÜLENMESİ

DOKTORA TEZİ

Tolga Ulaş GÜRBÜZ
(705072006)

İletişim Sistemleri Anabilim Dalı

Uydu Haberleşmesi ve Uzaktan Algılama Programı

Tez Danışmanı: Prof. Dr. İbrahim AKDUMAN

OCAK 2014

Tolga Ulaş Gürbüz, a **Ph.D.** student of ITU Informatics Institute student ID 705072006, successfully defended the **thesis** entitled "**NONLINEAR IMAGING OF DIELECTRIC OBJECTS BURIED UNDER A ROUGH SURFACE**", which he prepared after fulfilling the requirements specified in the associated legislations, before the jury whose signatures are below.

Thesis Advisor :	**Prof. Dr. İbrahim AKDUMAN** Istanbul Technical University	....
Jury Members :	**Prof.Dr. Ali YAPAR** Istanbul Technical University	....
	Assoc. Prof. Dr. Hülya ŞAHİNTÜRK Yıldız Technical University	....
	Prof.Dr. İrşadi AKSUN Koç University	....
	Assist. Prof. Dr. Serkan ŞİMŞEK İstanbul Technical University	....

Date of Submission : 4 December 2013
Date of Defense :   3 January 2014

To Çiğdem and Can,

FOREWORD

I would like to express my gratitudeto Prof. Ibrahim Akduman who continuously guided and supported me at every stage of this study and gave me the opportunity to work in an excellent scientific atmosphere with sparkling people.

All the former and current members of the Electromagnetics Research Group, in particular, Prof. Ali Yapar, Assoc. Prof. Hülya Şahintürk, Assist. Prof. Yasemin Altuncu, Assist. Prof. Pınar Karabulut, Assist. Prof. Serkan Şimşek, Assist. Prof. Mehmet Çayören, Birol Aslanyürek, Mehmet Abbak, Onan Güren, Evrim Tetik, Ahmet Hakan Tuncay, Fatih Erdem, Mehmet Nuri Akıncı, Nergis Erdem, Melike Erdoğan and Can Suer directly or indirectly contributed to this work; I deeply thank them all. I must seperately emphasize the important role of my friend and colleague Birol Aslanyürek in the emergence of the thesis in its present form.

I sincerely thank my parents Hasibe and Kemal and my brother Özgün for their continuous encouragement and faith in me. Finally and most importantly, I am grateful to my wife Çiğdem for everything. The fundamental elements that made this thesis possible are her infinite patience and unconditional support.

January 2014   Tolga Ulaş GÜRBÜZ

x

TABLE OF CONTENTS

ABBREVIATIONS

BOA   **:** Buried Object Approach
CG   **:** Conjugate Gradient
CSI   **:** Contrast Source Inversion
DBIM   **:** Distorted Born Iterative Method
DCIM   **:** Discrete Complex Images Method
FEM   **:** Finite Element Method
GPOF   **:** Generalized Pencil of Function
MoM   **:** Method of Moments
SNR   **:** Signal to Noise Ratio

LIST OF TABLES

xvii

LIST OF SYMBOLS

Γ : Surface of the rough interface
S : Measurement line
D : Reconstruction domain
T : Line of sources
C : Cross section of the buried object
ε : Dielectric permittivity
ε_r : Relative dielectric permittivity
σ : Conductivity
Ω : Angular frequency
$\boldsymbol{E}$: Electric field vector
$\boldsymbol{e_3}$: Unit vector in the Ox_3-direction
j : Indice of illuminations
u : Scalar field function
k : Wavenumber
χ : Contrast function
Δ : Laplace operator
$G(\boldsymbol{x}; \boldsymbol{y})$: Green's function for Helmholtz equation
δ : Dirac delta function
$G^{D,S}$: Integral operators
$\hat{G}$: Fourier transform of G
$H_0^{(1)}$: Zero order Hankel function of the first kind
Ψ : Spectral-domain counterparts of G
I : Identity operator
w : Contrast source
F : Cost functional
$\| . \|$: Euclidean norm
$\langle . , . \rangle$: Inner product
n : Indice of iterations
ρ : Data error
φ : Object error
d : Update directions for iterations
α : Step size for iterations
g : Gradient of the cost functional
G^{S*}, G^{D*} : Adjoints of operators G^S and G^D
$\bar{G}$: Complex conjugate of G
λ : Wavelength
η : Noise level
r_d : Uniformly distributed random variable

NONLINEAR IMAGING OF DIELECTRIC OBJECTS BURIED UNDER A ROUGH SURFACE

SUMMARY

Imaging of buried objects in a layered medium is a frequently encountared remote sensing problem and the use of microwaves for this purpose has been dealt with in many studies. In most of these studies, the inaccessible layer where an unknown object is presumed to be buried is illuminated by microwave antennas located in the accessible layer, and the scattered electromagnetic field that arises from the interaction of the incident wave with the object, as well as with the layer that hosts the object, is collected by receiving antennas. In the literature, there is a wide range of approaches to determine the geometrical and/or the material properties of the buried object by using the collected data. The vast majority of these approaches consider layered media with planar interfaces. On the other hand, although the problem is very important from both theoretical and practical points of view, very few studies deal with the imaging of dielectrics buried under a rough surface, and none of these studies apply one of the well accepted nonlinear inversion techniques to the problem despite the fact that most of these techniques are capable of reconstructing the dielectric profiles of inhomogeneous, even multiple, objects having sizes and complex permittivities in a relatively wide range.

In this thesis,a nonlinear tomographic approach for microwave imaging of dielectric objects buried under a rough surface is presented. The imaging problem is first reduced to the solution of a coupled system of integral equations which requires the knowledge of the Green's function of the layered background medium with rough interfaces. The required Green's function, as well as the contribution of the roughness to the total field, is calculated numerically via the Buried Object Approach (BOA) which suggests considering the roughness as a series of objects located alternately on both sides of a planar interface between two layers. The Green's function of the layered medium with planar interfaces, which is required in the application of the BOA, is accelerated through implementation of the two-level Discrete Complex Images Method (DCIM). Then the system of integral equations is solved for the contrast function associated with the object via the standard Contrast Source Inversion (CSI) method which is proven to be one of the most successful nonlinear inversion techniques when the Green's function of the background medium is available.By making use of the strength of nonlinear inversion and fast and accurate computation of the Green's function of the layered medium with rough interfaces, superior results have been achieved in a feasible computational time for dielectrics having constitutive parameters in a considerably wide range even if they are inhomogeneous or buried under substantially large rough surfaces.

ENGEBELİ BİR YÜZEY ALTINA GÖMÜLÜ DİELEKTRİK CİSİMLERİN DOĞRUSAL OLMAYAN YÖNTEMLERLE GÖRÜNTÜLENMESİ

ÖZET

Katmanlı bir ortama gömülü cisimlerin mikrodalgalar kullanılarak tespit edilmesi uzaktan algılama uygulamalarının önemli bir sınıfını oluşturmaktadır. Jeofizik etütler, yeraltı borularının ve tünellerin belirlenmesi, tahribatsız kontrol, tıbbi görüntüleme ve mayın tespit çalışmaları bu uygulamaların başlıca örnekleri olup,bir çoğunda, bilinmeyen cismin bulunduğu erişilemeyen katman, erişilebilen bir katmana yerleştirilen mikrodalga antenleriyle aydınlatılır ve gelen dalganın cisim ve cismin bulunduğu katman ile etkileşimi sonucu ortaya çıkan elektromagnetik alan erişilebilir katmandaki alıcı antenler kullanılarak ölçülür. Ölçülen bu alan,gömülü cismin geometrik veya elektromagnetik özelliklerinin farklı yöntemler aracılığıyla belirlenmesi için kullanılır. Bu doğrultuda, sentetik açıklıklı radar, doğrusal örnekleme, gradyan tabanlı optimizasyon yöntemleri, genetik ve memetik algoritmalar kullanılarak pek çok çalışma yapılmıştır. Ancak, bu çalışmaların neredeyse tamamında katmanlar arasındaki yüzeyin düzlemsel olduğu durum göz önüne alınmıştır. Oysa ki pratikte, belirlenmek istenen cismin gömülü olduğu katmanın yüzeyi çoğunlukla engebelidir ve bu durum problemi ciddi ölçüde etkileyerek görüntüleme işlemine yeni güçlükler getirir. Hem teorik, hem de pratik açıdan son derece önemli olmasına rağmen literatürde engebeli bir yüzey altına gömülü cisimlerin ele alındığı az sayıda çalışma mevcuttur. Bu çalışmaların önemli bir bölümünün amacı gömülü dielektrik veya metalik cisimlerin algılanmasıyla sınırlıyken,daha az sayıdaki bir grup çalışmadametalik cisimlerin görüntülenmesi için yöntemler önerilmektedir. Gömülü dielektrik cisimlerin geometrik ve elektromagnetik özelliklerinin birlikte belirlenerek görüntülenmesi problemiyle ilgilenen çalışmalar ise yok denecek kadar azdır. Bu çalışmalarda da görece düşük dielektrik sabitine sahip homojen cisimlerin hafif bir engebe altında görüntülenebildiği sınırlı sonuçlar elde edilmiştir. Bildiğimiz kadarıyla, geniş bir kompleks dielektrik sabiti aralığında,farklı geometrik özelliklere sahip homojen olmayansaçıcıların görüntülenmesinde oldukça etkin yöntemler oldukları bilinen doğrusal olmayan inversiyon yöntemlerinin engebeli yüzey altına gömülü dielektrik cisimlerin görüntülenmesi probleminde kullanıldığı bir çalışma bulunmamaktadır.

Bu tez çalışmasında, görüntülenmek istenen cismin bulunduğu uzaya ait Green fonksiyonunun bilinmesi halinde en etkili doğrusal olmayan inversiyon yöntemlerinden birisi olarak kabul edilen Kontrast Kaynak Inversiyon (Contrast Source Inversion, CSI) yönteminin engebeli yüzeyler altına gömülü dielektrik cisimlerin görüntülenmesi probleminde kullanılması sağlanmıştır.Bu amaçla, veri ve cisim denklemleri olarak adlandırılan ve bilinen bir uzayda bulunan cismin dielektrik özelliklerini cismin üzerinde alınan bir integral aracılığıyla ölçüm bölgesindeki ve cismin üzerindeki elektromagnetik alanla ilişkilendiren Fredholm tipi integral denklemler, görüntülenmek istenen cismin dışında kalan bütün yapıyı arka plan

olarak kabul ederek yazılmıştır. Bu durumda cismin görüntülenmesi problemi, bu iki integral denklemden, saçıcının dielektrik parametrelerinin fonksiyonu olan ve kontrast fonksiyonu adı verilen bir fonksiyonun elde edilmesi olarak ifade edilebilecek bir ters saçılma problemidir. Böylesi bir problem, kötü kurulmuş (ill-posed) ve doğrusal olmayan(nonlinear) bir problemdir ve literatürde belirli yaklaşıklıklara ve doğrusallaştırmalara dayalı farklı çözüm yöntemleri mevcuttur. Kontrast Kaynak Inversiyon yöntemi (CSI) bu amaçla önerilmiş olan ve aranan fonksiyonunbir hata fonksiyonelini minimize etmek üzere iteratif olarak güncellendiği ve bir değere yakınsanması halinde iterasyonun sonlandırıldığı bir doğrusal olmayan optimizasyon uygulamasıdır. Burada öncelikle integralin içinde çarpım şeklinde bulunan kontrast ve alan ifadeleri kontrast kaynağı adıyla tek bir değişken olarak tanımlanır. Veri denklemi bu tek değişkene göre doğrusal olmakla birlikte, denklemin kötü kurulmuş olması nedeniyle herhangi bir yöntem ile kontrast kaynağı için elde edilecek çözümün gerçek çözümden uzak olması beklenir. Öte yandan, denklem sisteminin gerçek bilinmeyenleri olan kontrast ve cismin üzerindeki alan açısından problemi ele aldığımızda da, cismin üzerindeki alanın kendisinin kontrasta bağlı olması nedeniyle problemin doğrusal olmayan (nonlinear) bir problem olduğunu görürüz. Literatürde Born yaklaşıklığı (Born approximation) adı verilen yaklaşıma göre cismin üzerindeki alan gelen alana eşit kabul edilerek denklem kontrast için doğrusal hale getirilebilir. Ancak söz konusu kabul ve doğrusallaştırma yalnızca zayıf saçıcılarda mümkün olmaktadır. Dolayısıyla geniş bir kompleks dielektrik sabiti ve boyut bölgesinde çözüm verebilecek bir görüntüleme yaklaşımı için problemin doğrusal olmayan karakterinin göz ardı edilmemesi gerekir. Bu çerçevede CSI yönteminde, herhangi bir doğrusallaştırma yapmaksızın,çözümü ararken cisim denklemini de göz önüne alarak bir minimizasyon gerçekleştirmek amacıyla, hata fonksiyoneli veri ve cisim denklemlerinin hatalarının toplamı şeklinde ifade edilir ve bu toplamı birlikte minimize edecek kontrast kaynağı ve kontrast büyüklükleri dönüşümlü olarak güncellenerek iterasyon gerçekleştirilir.Böylesi bir yöntem, iterasyonun her adımında düz problemin çözümüne ihtiyaç duyulmaması ve her adıma ilişkin ifadeyi minimize eden kontrast büyüklüğünün analitik olarak belirleniyor olması ile benzer yöntemlerden ayrılır ve literatürde bilinen en etkili doğrusal olmayan inversiyon yöntemlerinden biridir. Ancak genel halde, söz konusu yöntemin çözümünü aradığı veri ve cisim denklemlerindeki integrallerin çekirdeğinde, cismin bulunduğu arka plana ilişkin Green fonksiyonu yer almaktadır ve problem formülasyonunun bu çalışmada önerildiği gibi ifade edilmesi halinde,bu arka planengebeli bir yüzey ile bölünmüş katmanlı uzaydır. Bu uzaya ilişkin Green fonksiyonunun değerinin analitik olarak hesaplanması mümkün olmamakla birlikte, Gömülü Cisim Yaklaşımı (Buried Object Approach, BOA) adı verilen bir yaklaşım ile sayısal olarak ihtiyaç duyulan Green fonksiyonu elde edilebilir. Buna göre, engebeli yüzeyin girinti ve çıkıntıları, düzlemsel bir arayüzle birbirinden ayrılmış iki yarı-uzaya gömülmüş cisimler gibi düşünülür ve ihtiyaç duyulan noktalara yerleştirilen noktasal kaynaklara ilişkin alanlar Momentler Yöntemi (Method of Moments, MoM) kullanılarak sentetik olarak elde edilir. Bu alan büyüklükleriaranılan Green fonksiyonunun değerleridir. Böylesi bir yaklaşımın ise düzlemsel bir arayüzle ayrılmış katmanlı uzaya ilişkin Green fonksiyonuna ihtiyaç duyduğu açıktır. Bu Green fonksiyonu, çekirdeğinde spektral yansıma ve iletim katsayılarının yer aldığı sonsuz integraller şeklinde yazılabilmektedir. Bu integrallerin sayısal olarak hesaplanması mümkün olsa da, integralin çekirdeğinin mikrodalgalardaki aşırı salınımlı ve yavaş azalan yapısı nedeniyle bu, oldukça zaman alıcı olmaktadır. Bu nedenle literatürde,bazı yaklaşıklarla bu integralleri hesaplayan

yöntemler önerilmiştir. Ayrık Karmaşık Görüntüler Yöntemi (Discrete Complex Images Method, DCIM) bu yöntemlerin en etkililerinden biri olup esas olarak integralin çekirdeğindeki spektral katsayıların karmaşık üstel fonksiyonların toplamı olarak ifade edilmesi ve böylece hesaplanmak istenen Green fonksiyonunun, boş uzay Green fonskiyonunun bilinen integral gösterilimi göz önüne alınarak, argümanı kompleks terimler içeren boş uzay Green fonksiyonlarının toplamı olarak yazılabilmesidir.

Doğrusal olmayan inversiyonun etkinliği ve engebeli bir arayüze sahip katmanlı uzayın Green fonkiyonunun Gömülü Cisim Yaklaşımı (Buried Object Approach, (BOA) ve Ayrık Karmaşık Görüntüler Yöntemi (Discrete Complex Images Method, DCIM) birlikte kullanılarak hızlı ve doğru bir biçimde hesaplanması sayesinde, önerilen yöntem ile, verinin ölçüm düzeneğinden kaynaklanan doğal eksikliğine rağmen ve makul bir süre içerisinde oldukça başarılı sonuçlar elde edilebilmektedir. Farklı simülasyonlarda görülmüştür ki, önerilen yöntem, homojen olmayan dielektrik cisimlerin geniş bir bölgede değişiklik gösteren dielektrik parametrelerini elde etmeye olanak vermektedir. Dahası yöntem, engebeli yüzeyin boyutlarındaki artıştan diğer yöntemlere göre çok daha az etkilenmektedir ve oldukça yüksek engebeli yüzeylerin altındaki cisimler de başarıyla görüntülenebilmektedir. Simülasyonlar tek bir frekansta gerçekleştirilmiştir ve frekansın arzu edilen çözünürlüğünve cismin boyutunun izin verdiği ölçüde azaltılması özellikle derindeki cisimler için görüntüleme sonuçlarını iyileştirmektedir.

1. INTRODUCTION

1.1 Purpose of the Thesis

Microwave detection or imaging of objects buried in a layered medium constitutes an important class of problems in remote sensing applications such as geophysical exploration, nondestructive testing, determination of underground pipes and tunnels, medical imaging, mine detection, etc. In most of these applications,an inaccessible layer in which an unknown object is presumed to be buried is illuminated by microwave antennas located in another layer. Then, the scattered electromagnetic field that arises from the interaction of the incident wave with the object, as well as with the layer that hosts the object, is collected by receiving antennas located in the accessible layer. The collected data are used to determine the geometrical and/or the material properties of the object by using different approaches. Mostly, the objects to be detectedare dielectric and buried in layered media having rough interfaces. Hence,the purpose of this thesis is to give a fast and efficient methodology fordetermination of both geometrical and electromagnetic properties of dielectric objects buried in layered medium having rough interfaces.

1.2 Literature Review

A wide range of approaches, which use, among others, modified gradient method [1], [2] standard or modified Born iterative methods [3], [4] first or higher order Born approximations [5]–[7] distorted Born iterative method [8], [9], linear sampling method [10], synthetic aperture technique [11], genetic or memetic algorithms [12]–[14], have been introduced during the last two decades for determination of the geometrical or material properties of objects buried in a layered medium. The vast majority of these approaches consider layered media that contains planar interfaces only. However,in most of thereal applications, objects to be reconstructedare buried in layered media having rough interfaces. In such cases, the roughness of theinterface significantly affects the scattering phenomena and brings new difficulties to the

imaging procedure. In the open literature, one can find some studies that deal with the inverse scattering problem associated with objects buried under rough surfaces. In [15], a method based on the determination of the surface impedance on the rough interface through the standard impedance boundary condition is presented. Statistical averages of Mueller and covariance matrix elements, which are obtained by direct simulations for rough ground with and without buried objects, are used to determine signatures of buried dielectrics in [16] and [17], respectively. The application of angular correlation function processing when a metallic object is sought by ground penetration radar is investigated in [18] while a method based on a correlation of the scattered fields from two sets of data associated with two transmitters is given in [19]. The works listed above are concerned with the detection of dielectric or metallic objects. On the other hand, for buried conductors, some imaging approaches such as the ones that use time reversal method [20] and synthetic aperture radar [21] are proposed.

Although the problem is very important from both theoretical and practical points of view, very few studies deal with the imaging of dielectrics buried under a rough surface. In [22], an approach based on analytical continuation as well as on reciprocity gap linear sampling method is applied for shape reconstruction and localization of buried dielectrics under a slightly varying rough surface. Similarly, a dielectric with a known permittivity is imaged by applying a level-set algorithm in [23]. An iterative method based on the semi-analytic mode matching forward model is proposed in [24]. The method allows reconstruction of a homogeneous object having relatively low dielectric permittivity as well as of the roughness of the surface when the surface has a very slight variation. An early attempt for inhomogeneous dielectric profile reconstruction of buried objects is given in [25]. A very primitive and basic method, i.e. an application of the Method of Moments (MoM) which is mostly used in the solution of direct scattering problems, is applied to reconstruct the objects. As might be expected, although noise-free data are used, the reconstruction results are far from being satisfactory even for low permittivity dielectrics.

As far as we know, except [26] which is a preliminary study of our research group, there is no study that applies one of the well accepted nonlinear inversion techniques for imaging of dielectrics buried under a rough surface although most of these techniques are capable of reconstructing the dielectric profiles of inhomogeneous,

even multiple, objects having sizes and complex permittivities in a relatively wide range. In [26], the Distorted Born Iterative Method (DBIM) is applied in conjunction with the Buried Object Approach (BOA) [27], which enables calculation of the Green's function of layered media with rough interfaces by considering the roughness as a series of objects located alternately on both sides of a planar interface between two half-spaces. On the other hand, since the Green's function of the two-layered media with a planar interface required in the application of the BOA is computed by direct numerical integration of the spectral integrals of infinite extend and the DBIM has many parameters whose particular selection has significant impacts on the computational cost of the method as well as on the quality of the reconstructions [28], the procedure given in [26] is impractical to be used in real applications for a wide range of geometries and material properties. Hence, marginal results are achieved in [26] even for considerably low values of the size of the roughness as well as of the dielectric parameters of the soil and the object.

1.3 Significance of the Study

In this study, a nonlinear inversion technique is effectively applied to the problem of microwave imaging of buried dielectrics under a rough surface for the first time.More precisely,it has been made possible to efficiently apply the Contrast Source Inversion (CSI) method, which is proven to be one of the most successful nonlinear inversion techniques when the Green's function of the background medium is available, to the problem. This has been achieved through the application of the BOA in conjunction with an adaptation of the two-level Discrete Complex Images Method (DCIM), which is an effective method that eliminates the need for numerical integration required for the calculation of the Green's function of the two-layered media with a planar interface.

By making use of the strength of nonlinear inversion and fast computation of the Green's function of the layered media with rough interface, the proposed approach yields superior results in a feasible computational time despite the incomplete data resulting from the nature of the subsurface imaging problem. It has been confirmed through various simulations that the approach is capable of reconstructing even inhomogeneous dielectrics having constitutive parameters in a considerably wide range. Moreover, it is much less affected by increased size of the roughness and

objects buried under substantially large rough surfaces are successfully imaged. The simulations have been performed at single frequency and it has been observed that lowering the operation frequency to an extent permitted by the size of the object and the desired spatial resolution improves the performance of the method especially for the objects in deeper locations.These results indicate that the proposed approach has a strong potential to be adapted to real remote sensing applications from different fields which require reconstruction of both the geometrical and material properties of buried objects under a rough surface.

1.4 Organization of the Thesis

The organization of the thesis is as follows. The statement of the imaging problem is given in Section 2. Section 3 is devoted to the calculation of the Green's function of the background medium while the inversion procedure is explained in Section 4. Some numerical results and conclusions are presented in Section 5 and Section 6 respectively.

Throughout the thesis, the exp(-iωt) time factor is suppressed, vectors are denoted by bold letters and complex conjugate is denoted by overbar.

2. STATEMENT OF THE IMAGING PROBLEM

2.1 Geometry of the Problem

In the case that the geometry is uniform along the Ox_3-direction, the problem of imaging an unknown object which is known to lie under a rough surface can be treated as a two-dimensional problem on the Ox_1x_2 plane as shown in Figure 2.1. In this configuration, two half-spaces are separated by a locally rough interface Γ whose coordinates (x_1^Γ, x_2^Γ) can be determined through the relation

$$x_2^\Gamma = \begin{cases} f(x_1^\Gamma), & x_1^\Gamma \in L \\ 0, & x_1^\Gamma \in \mathbb{R} \setminus L \end{cases} \qquad (2.1)$$

where f is a single valued function and subset $L \subset \mathbb{R}$ is the finite interval over which the interface deviates from a flat surface. The homogeneous half-spaces $x_2 > f(x_1)$ and $x_2 < f(x_1)$ are composed of simple materials with constitutive parameters ε_1, σ_1 and ε_2, σ_2 respectively. In the lower half-space, an infinitely long cylindrical object having a cross-section C with the Ox_1x_2 plane is located. The dielectric permittivity and the conductivity of the inhomogeneous object are $\varepsilon_C(\boldsymbol{x})$ and $\sigma_C(\boldsymbol{x})$ respectively, where $\boldsymbol{x} = (x_1, x_2)$ is the position vector in $\mathbb{R}^2$. Note that, the magnetic permeabilities of the half-spaces and the object areequal to the vacuum permeability μ_0.

In the imaging approach given here, the region in which the objects are assumed to be located is successively illuminated by microwave sources at the points $\boldsymbol{z}_j$, $j = 1, 2, \ldots, J$, on line T and for each illumination the total electric field vector is measured on line S (seeFigure 2.1). The electric field vector of each incident wave, which is time-harmonic with angular frequency ω, is $\boldsymbol{E}_i(\boldsymbol{x}; \boldsymbol{z}_j) = u_i(\boldsymbol{x}; \boldsymbol{z}_j)\boldsymbol{e_3}$where $\boldsymbol{e_3}$is the unit vector in the Ox_3-direction. Then, the problem can be reduced to a scalar one in terms of the field function $u_j(\boldsymbol{x})$ which represents the total electric field vector $\boldsymbol{E}(\boldsymbol{x}; \boldsymbol{z}_j) = u(\boldsymbol{x}; \boldsymbol{z}_j)\boldsymbol{e_3}$ in $\mathbb{R}^2$ for the jth illumination. The inverse scattering

problem considered here is to determine the location and shape as well as the constitutive parameters of the object by using the measured field, namely $u_j(x)$ for $x \in S$. Although there is no objection to the extension of the proposed approach to more general 3D and multi-layered structures, for the sake of simplicity, we restrict our attention to 2D and two-layered structures in this study.
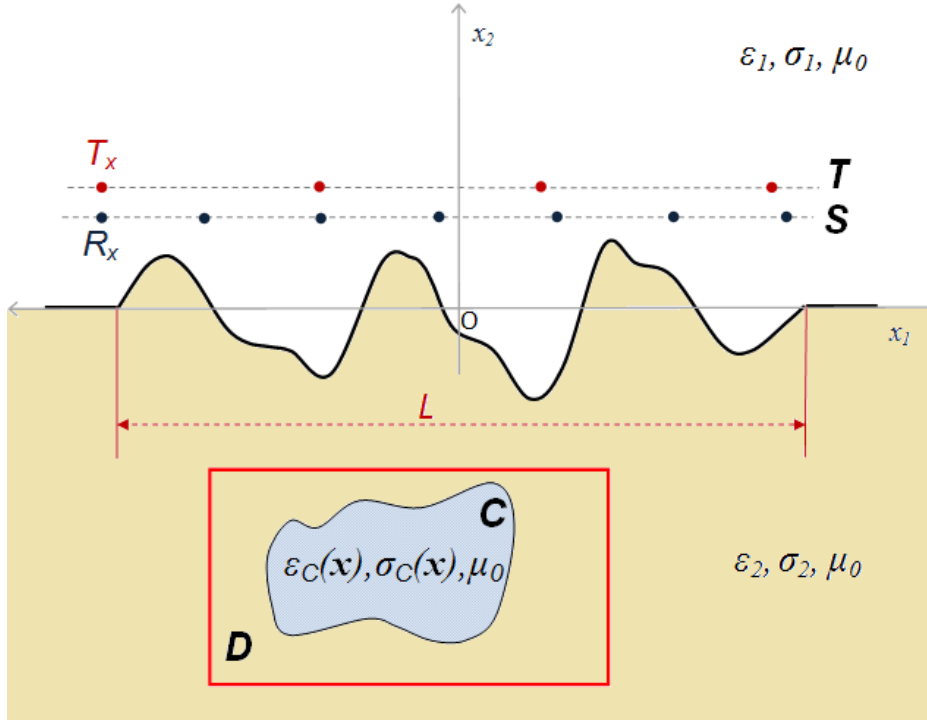
Figure 2.1 : Geometry of the problem.

2.2 Formulation of the Problem

The total field $u_j(x)$ can be considered as $u_j(x) = u_{b,j}(x) + u_{s,j}(x)$, where the *background field* $u_{b,j}(x)$ is the total field for the *j*th illumination in the absence of the object and $u_{s,j}(x)$ is the field scattered from the object. $u_{b,j}(x)$ could be obtained through a simulation performed by using a computational electromagnetics technique or, if possible, through a pre-measurement performed in the absence of the object. In the source-free region, this field satisfies the homogeneous Helmholtz equation

$$\Delta u_{b,j}(x) + k_b{}^2(x)u_{b,j}(x) = 0 \tag{2.2}$$

where $k_b(x)$ is the wave-number of the background medium in the absence of the object, and its square is given by

$$k_b{}^2(x) = \begin{cases} k_1^2 = \omega^2 \varepsilon_1 \mu_0 + i\omega\sigma_1\mu_0, & x_2 > f(x_1) \\[2mm] k_2^2 = \omega^2 \varepsilon_2 \mu_0 + i\omega\sigma_2\mu_0 x_2 < f(x_1). \end{cases} \qquad (2.3)$$

On the other hand, the total field u_j satisfies

$$\Delta u_j(x) + k^2(x)u_j(x) = 0 \qquad (2.4)$$

in the source-free region. In this case, the propagation medium includes the object, and hence the square of the wave-number $k(x)$ is

$$k^2(x) = \begin{cases} \omega^2 \varepsilon_C(x)\mu_0 + i\omega\sigma_C(x)\mu_0, & x \in C \\[2mm] k_b{}^2(x), & x \notin C. \end{cases} \qquad (2.5)$$

By adding the term $k_b{}^2(x)u_j(x) - k_b{}^2(x)u_j(x)$ to the left side of (2.4), and with the aid of (2.2) and $u_j(x) = u_{b,j}(x) + u_{s,j}(x)$, we obtain

$$\Delta u_{s,j}(x) + k_b{}^2(x)u_{s,j}(x) = -k_b{}^2(x)\chi(x)u_j(x) \qquad (2.6)$$

where $\chi(x)$ is the contrast function related to the object and is defined by

$$\chi(x) = \frac{k^2(x)}{k_b{}^2(x)} - 1. \qquad (2.7)$$

Note that, if the illuminations were performed in different frequencies the value of the contrast function at any point x would change with the illuminations since it is a function of the frequency. However, single frequency is considered in this study and thus the contrast function is same for all illuminations. For this reason, the index j is not used for the contrast χ throughout the thesis. Equation (2.6) is the inhomogeneous Helmholtz equation thatgoverns the propagation of the scattered field. Here, the object is represented with the source term $-k_b{}^2(x)\chi(x)u_j(x)$, and the scattered field $u_{s,j}(x)$ is represented as a field radiating from this source in the medium defined by $k_b(x)$. This field also satisfies the Sommerfeld radiation

condition

$$\lim_{r\to\infty} r^{1/2}\left(\frac{\partial u_{s,j}(\boldsymbol{x})}{\partial r} - ik_b(\boldsymbol{x})u_{s,j}(\boldsymbol{x})\right) = 0, \qquad r = |\boldsymbol{x}|, \qquad (2.8)$$

which in general states that the energyradiated from the sources must scatter to infinity [29] and in practice ensures the uniqueness of the solution to the scattering problemby choosing the outgoing wave from possible solutions of the Helmholtz equation [30].

In order to solve the scattering problem given by(2.6) and (2.8), the Green's function of the background medium $G_b(\boldsymbol{x};\boldsymbol{y})$ is defined as the total field due to a line source, which satisfies

$$\Delta G_b(\boldsymbol{x};\boldsymbol{y}) + k_b{}^2(\boldsymbol{x})G_b(\boldsymbol{x};\boldsymbol{y}) = -\delta(\boldsymbol{x}-\boldsymbol{y}). \qquad (2.9)$$

as well as the radiation condition. In [30] it is proved that through the Green's function $G_b(\boldsymbol{x};\boldsymbol{y})$, one can write the scattered field $u_{s,j}(\boldsymbol{x})$ that satisfies both (2.6) and (2.8) in an integral form as

$$u_{s,j}(\boldsymbol{x}) = \iint_C G_b(\boldsymbol{x};\boldsymbol{y})k_b{}^2(\boldsymbol{y})\chi(\boldsymbol{y})u_j(\boldsymbol{y})d\boldsymbol{y}, \qquad (2.10)$$

which enables to obtain the field scattered from the object at any point$\boldsymbol{x}$by integrating the "source" values on the object. On the other hand, it is clear from (2.10) that the values of the total field u_j on the object are required. Since (2.10) is valid at any point and $u_j(\boldsymbol{x}) = u_{b,j}(\boldsymbol{x}) + u_{s,j}(\boldsymbol{x})$, we can write the equation

$$u_j(\boldsymbol{x}) = u_{b,j}(\boldsymbol{x}) + \iint_C G_b(\boldsymbol{x};\boldsymbol{y})k_b{}^2(\boldsymbol{y})\chi(\boldsymbol{y})u_j(\boldsymbol{y})d\boldsymbol{y}, \qquad \boldsymbol{x}\in C, \qquad (2.11)$$

which is known as the Lippmann-Schwinger equation. From (2.10) and (2.11), one can obtain the scattered field at any point by applying the Method of Moments (MoM) procedure given in [34] when the contrast function χ, namely the constitutive parameters of the object, are known.

In the inverse scattering problem, which is the subject of this study, both the dielectric property values and the cross-section C of the object are unknown while the total field $u_j(\boldsymbol{x})$ and consequently $u_{s,j}(\boldsymbol{x})$, on the measurement line S are known. In this case, regarding the fact that the contrast function χ given in (2.7) vanishes for $\boldsymbol{x} \notin C$, we can consider a reconstruction domain D which is chosen large enough to contain the unknown object as shown in Figure 2.1 and perform the integrations in (2.10) and (2.11) on D instead of C. Accordingly, the total field u_j appearing in the integrals is needed to be defined for $\boldsymbol{x} \in D$. The resulting integral equations can be symbolically written as

$$u_j = u_{b,j} + G^D \chi u_j, \qquad \boldsymbol{x} \in D, \qquad j = 1, 2, \ldots, J \qquad \textbf{(2.12)}$$

$$u_{s,j} = G^S \chi u_j, \qquad \boldsymbol{x} \in S, \qquad j = 1, 2, \ldots, J \qquad \textbf{(2.13)}$$

where G^D is an integral operator mapping from $L^2(D)$ into $L^2(D)$ and G^S is an operator mapping from $L^2(D)$ into $L^2(S)$. These operators are given by

$$(G^{D,S}\psi)(\boldsymbol{x}) = \iint_D G_b(\boldsymbol{x};\boldsymbol{y}) k_b{}^2(\boldsymbol{y})\psi(\boldsymbol{y})d\boldsymbol{y}, \quad \boldsymbol{x} \in D, S. \qquad \textbf{(2.14)}$$

Equations (2.12) and (2.13) are known as the *object* and *data* equations, respectively and the imaging problem can be expressed as the extraction of χ from these equations since its real and imaginary parts are related to the constitutive parameters of the object, namely $\varepsilon_C(\boldsymbol{x})$ and $\sigma_C(\boldsymbol{x})$. This problem is nonlinear with respect to χ, and a solution through the Constrast Source Inversion (CSI) method [33] is given in Section 4. Before going further, it is convenient to give a method for fast and accurate computation of $G_b(\boldsymbol{x};\boldsymbol{y})$ appearing in (2.12) and (2.13).

3. THE GREEN'S FUNCTION OF THE BACKGROUND MEDIUM

3.1 Buried Object Approach

In order to solve the inverse scattering problem given by (2.12) and (2.13), one needs to know the Green's function of the background, namely $G_b(x; y)$, for relevant pairs of x and y. This could be achieved by the application of the Buried Object Approach (BOA). According to this approach, the elevations of the rough surface are considered as N cylindrical objects lying in the $x_2 > 0$ half-space with cross-sections $B_1, B_3, \ldots, B_{2N-1}$ and constitutive parameters ε_2, σ_2 as shown in Figure 3.1. Similarly, the depressions of the ground are treated as N cylindrical objects lying in the $x_2 < 0$ half-space with cross-sections $B_2, B_4, \ldots, B_{2N}$ and constitutive parameters ε_1, σ_1. In other words, the entire roughness is considered as a scatterer whose constitutive parameters vary with position in the region $B = B_1 \cup B_2 \ldots \cup B_{2N}$.
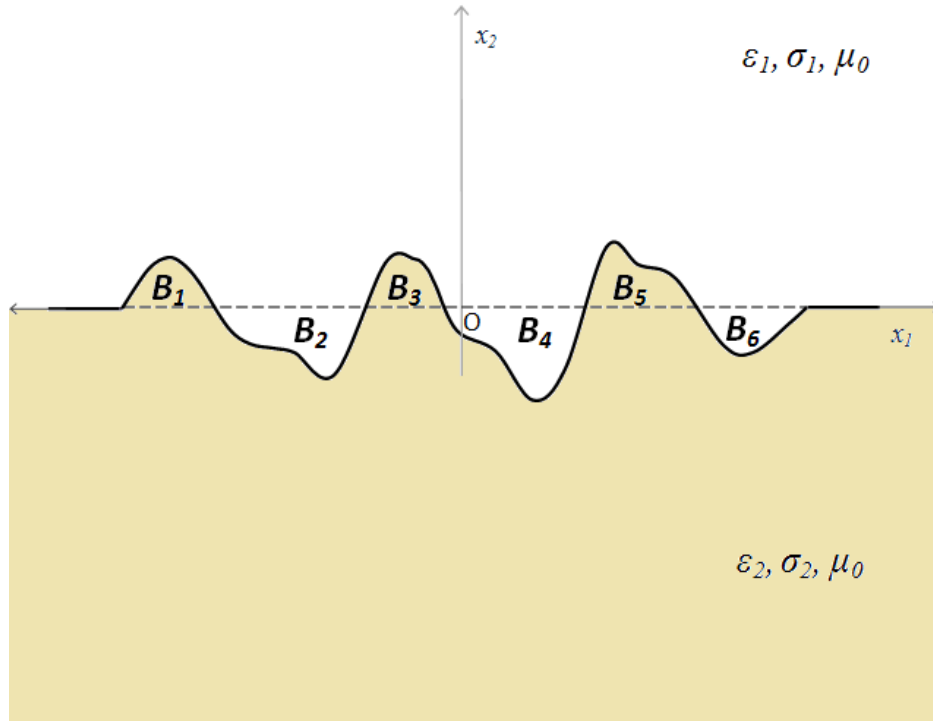

Figure 3.1 : Representation of the background medium according to the BOA.

In this case, $G_b(x; y)$ can be obtained by separating it into two components as

$$G_b(x; y) = G_B(x; y) + G_{12}(x; y) \qquad (3.1)$$

where $G_{12}(x; y)$ is the Green's function of the two-layered media with a planar interface while $G_B(x; y)$ is the contribution of the roughness. Here, $G_B(x; y)$ can be considered as the scattered field from the so-called objects that represent the roughness due to a line source of unit strength located at point y. Accordingly, we can write the integral equation for the Green's function of the background, i.e. $G_b(x; y)$, considering it as the total field due to a line source of unit strength located at point y. In this case, $G_{12}(x; y)$ will be the incident field while $G_B(x; y)$ is the scattered field from the so-called objects that represent the roughnes. The integralequation governing such a scattering process can be written as

$$G_b(x; y) = G_{12}(x; y) + \iint_B G_{12}(x; z)\left(k_b{}^2(z) - k_{12}^2(z)\right) G_b(x; y)dz. \quad (3.2)$$

From (3.1) and (3.2), $G_B(x; y)$ satisfies the integral equation

$$(I - Q)G_B(x; y) = QG_{12}(x; y) \qquad (3.3)$$

where the integral operator Q is defined by

$$(QG)(x; y) = \iint_B G_{12}(x; z)\left(k_b{}^2(z) - k_{12}^2(z)\right) G(z; y)dz. \qquad (3.4)$$

In (3.4), $k_{12}(x)$ is the wave-number of the two-layered media with a planar interface and its square is given by

$$k_{12}^2(x) = \begin{cases} k_1^2, & x_2 > 0 \\ k_2^2, & x_2 < 0. \end{cases} \qquad (3.5)$$

Equation(3.3) can be solved for $G_B(x; y)$ by adaptingthe forward solution procedure given in [34].

12

3.2 The Green's Function of theTwo-Layered Media with a Planar Interface

3.2.1 Integral represantation of the Green's function

It is clear that the solution of (3.3) requires $G_{12}(x; y)$ which is the total field due to a line source of unit strength located at point y in the two-layered media with a planar interface shown in Figure 3.2.

$$\varepsilon_1, \sigma_1, \mu_0$$

x_2

O

x_1

$$\varepsilon_2, \sigma_2, \mu_0$$
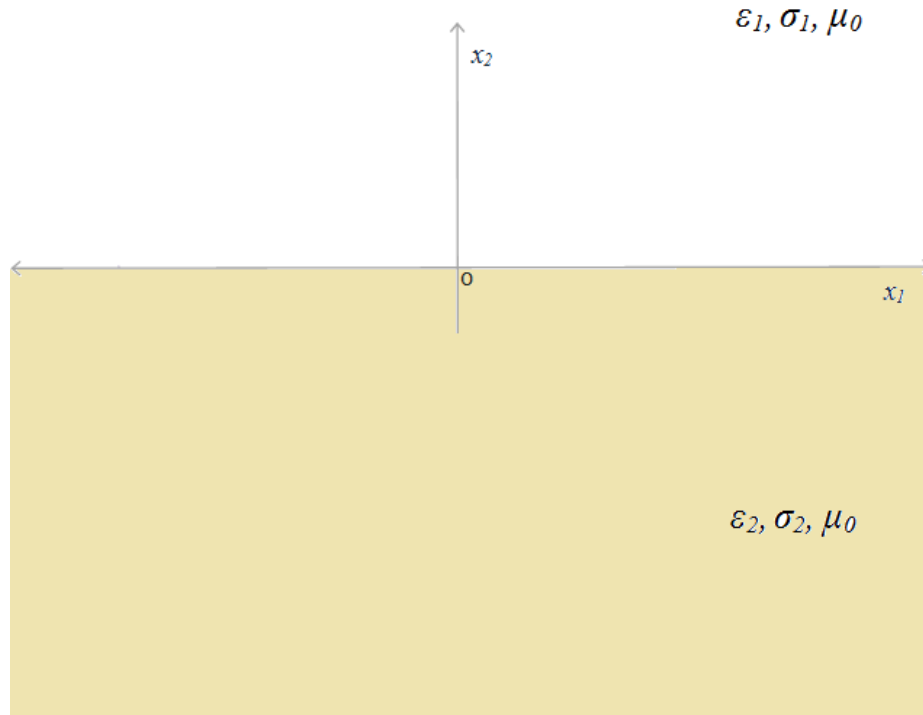
Figure 3.2: The two-layered media with a planar interface.

By definition, $G_{12}(x; y)$ satisfies the Helmholtz equation

$$\Delta G_{12}(x; y) + k_{12}{}^2(x)G_{12}(x; y) = -\delta(x - y), \qquad (3.6)$$

along with the boundary conditions at $x_2 = 0$ which are given as

$$G_{12}|_{x_2=0+\xi} = G_{12}|_{x_2=0-\xi} \qquad as \ \xi \to 0_+,$$

$$\left.\frac{\partial G_{12}}{\partial x_2}\right|_{x_2=0+\xi} = \left.\frac{\partial G_{12}}{\partial x_2}\right|_{x_2=0-\xi} \qquad as \ \xi \to 0_+$$

$$(3.7)$$

and the Sommerfeld radiation condition.

Since the discontinuity of the medium is along Ox_2-direction, we take the Fourier transform of (3.6) with respect to x_1 in order to deal with the problem in the Ox_2-direction only and obtain

$$\frac{\partial^2 \hat{G}_{12}}{\partial x_2^2} - \left(v^2 - k_{12}{}^2\right)\hat{G}_{12} = -e^{-ivy_1}\delta(x_2 - y_2), \qquad (3.8)$$

where $\hat{G}_{12}$ is the Fourier transform of G_{12} defined by

$$\hat{G}_{12}(v, x_2; \boldsymbol{y}) = \int\limits_{-\infty}^{\infty} G_{12}(\boldsymbol{x}; \boldsymbol{y})e^{-ivx_1}dx_1. \qquad (3.9)$$

In this case, from (3.8), we have boundary conditions at $x_2 = y_2$ for $\hat{G}_{12}$ which are

$$\hat{G}_{12}\Big|_{x_2=y_2+\xi} = \hat{G}_{12}\Big|_{x_2=y_2-\xi} \qquad as\ \xi \to 0_+,$$

$$\frac{\partial \hat{G}_{12}}{\partial x_2}\Big|_{x_2=y_2+\xi} - \frac{\partial \hat{G}_{12}}{\partial x_2}\Big|_{x_2=y_2-\xi} = -e^{-ivy_1}as\ \xi \to 0_+.$$

$$(3.10)$$

In addition, at $x_2 = 0$, $\hat{G}_{12}$ satisfies the Fourier transforms of the conditions given in (3.7) which are

$$\hat{G}_{12}\Big|_{x_2=0+\xi} = \hat{G}_{12}\Big|_{x_2=0-\xi} \qquad as\ \xi \to 0_+,$$

$$\frac{\partial \hat{G}_{12}}{\partial x_2}\Big|_{x_2=0+\xi} = \frac{\partial \hat{G}_{12}}{\partial x_2}\Big|_{x_2=0-\xi} \qquad as\ \xi \to 0_+.$$

$$(3.11)$$

By using (3.10) and (3.11) along with the Sommerfeld radiation condition, (3.8) can be solved for $\hat{G}_{12}$ and, after applying the inverse Fourier transform, G_{12} can be written as

$$G_{12}(x; y) = \begin{cases} G_0(x; y) + G_1(x; y), & x_2 > 0, y_2 > 0 \\ G_2(x; y), & x_2 < 0, y_2 > 0 \\ G_3(x; y), & x_2 > 0, y_2 < 0 \\ G_0(x; y) + G_4(x; y), & x_2 < 0, y_2 < 0 \end{cases}$$

(3.12)

where G_0 is the direct part of the Green's function of the two-layered media with a planar interface while $G_{1,4}$ and $G_{2,3}$ are the reflected and the transmitted parts respectively. G_0 can be written as

$$G_0(x; y) = \frac{i}{4} H_0^{(1)}(k_{12}(x)|x - y|)$$

(3.13)

with $H_0^{(1)}$ being the zero order Hankel function of the first kind. On the other hand, there are no closed-form expressions for $G_{1,4}$ and $G_{2,3}$ which are obtained by taking the inverse Fourier transforms

$$G_p(x; y) = \frac{1}{2\pi} \int_{C_R} \hat{G}_p e^{ivx_1} dv, \quad p = 1, 2, 3, 4.$$

(3.14)

Here, $\hat{G}_p$ represents the reflected or transmitted parts of $\hat{G}_{12}$ depending on the regions of both the observation and source points. These parts are explicity obtained as

$$\hat{G}_1 = \frac{1}{2\gamma_1} \Psi_1(v) e^{-\gamma_1(x_2 + y_2)} e^{-ivy_1},$$

$$\hat{G}_2 = \frac{1}{2\gamma_1} \Psi_2(v; x_2) e^{-\gamma_1 y_2} e^{-ivy_1},$$

$$\hat{G}_3 = \frac{1}{2\gamma_2} \Psi_3(v; x_2) e^{\gamma_2 y_2} e^{-ivy_1},$$

$$\hat{G}_4 = \frac{1}{2\gamma_2} \Psi_4(v) e^{\gamma_2(x_2 + y_2)} e^{-ivy_1},$$

(3.15)

where

$$\Psi_1(v) = \frac{\gamma_1(v) - \gamma_2(v)}{\gamma_1(v) + \gamma_2(v)},$$

$$\Psi_2(v; x_2) = \frac{2\gamma_1(v)}{\gamma_1(v) + \gamma_2(v)} e^{\gamma_2 x_2},$$

$$\Psi_3(v; x_2) = \frac{2\gamma_2(v)}{\gamma_1(v) + \gamma_2(v)} e^{-\gamma_1 x_2},$$

$$\Psi_4(v) = \frac{\gamma_2(v) - \gamma_1(v)}{\gamma_1(v) + \gamma_2(v)},$$

(3.16)

with

$$\gamma_1(v) = \sqrt{v^2 - k_1^2}, \qquad \gamma_2(v) = \sqrt{v^2 - k_2^2}. \qquad (3.17)$$

The square root functions appearing in (3.17) are defined in the complex v-plane with the conditions

$$\gamma_q(0) = -ik_q, \qquad q = 1,2. \qquad (3.18)$$

The integration path C_R of the infinite integral (3.14) is given in Figure 3.3.
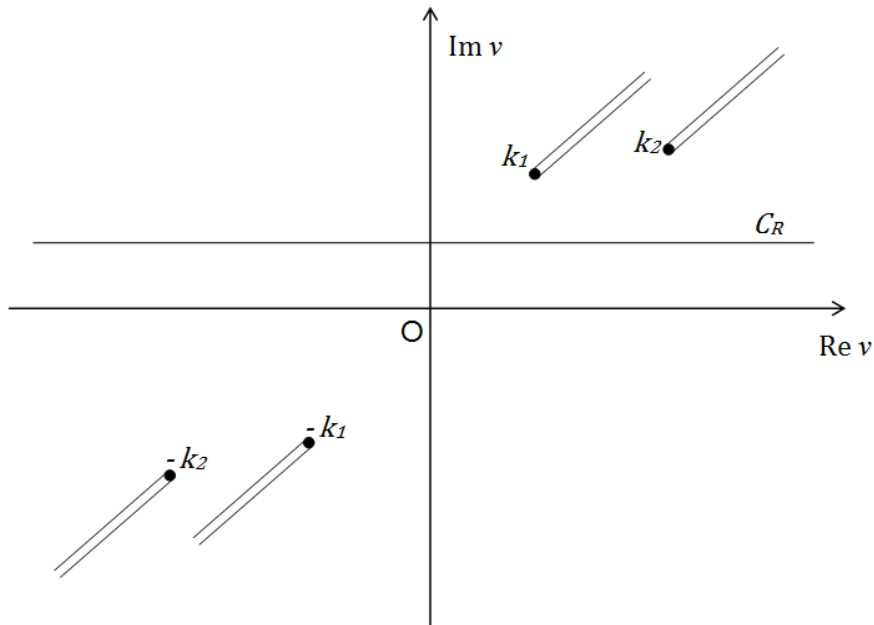

Figure 3.3: The integration path C_R of the infinite integral.

Note that, (3.14) cannot be evaluated analytically and in most cases, direct evaluation of the integral with any numerical quadrature technique is computationally very expensive and is not robust due to the highly oscillatory and slowly converging behavior of the integrand especially for the reflected parts. In order to overcome this difficulty, many different approaches are proposed in the literature [35], [36]. The Discrete Complex Images Method (DCIM) [37] is one of the most efficient of these approaches and hence has been adapted to the problem as summarized below.

3.2.2 Two-level discrete complex images method

According to the Discrete Complex Images Method (DCIM) , an appropriate part of the spectral integrand is sampled along the integration path and approximated in terms of complex exponentials by using an exponential fitting algorithm such as the Generalized Pencil of Function (GPOF) method [38]. Then, one can obtain approximate closed-form expressions in the spatial-domain through the integral representation of the scalar free space Green's function. In an improved version of this method, which is given in detail in [31], [32], the integration path is split into two parts over which separate exponential approximations are performed in a semi-independent manner. This two-level approach is implemented in the present problemand Ψ_p functions given in (3.16) are approximated as a sum of two series of exponentials as

$$\Psi_p \cong \sum_{n=1}^{N_p^{\{1\}}} a_{n,p} e^{ib_{n,p}\gamma_q} + \sum_{n=1}^{N_p^{\{2\}}} c_{n,p} e^{id_{n,p}\gamma_q} \tag{3.19}$$

provided $q = 1$ for $p = 1,2$ and $q = 2$ for $p = 3,4$. Here, $a_{n,p}$, $b_{n,p}$ and $c_{n,p}$, $d_{n,p}$ are the coefficients obtained from the approximations performed along the first and second parts of the integration path, respectively, while the corresponding numbers of exponentials are $N_p^{\{1\}}$, $N_p^{\{2\}}$. Then, by considering the integral representation of the Hankel function, namely

$$\frac{i}{4} H_0^{(1)}\big(k_q|\boldsymbol{x} - \boldsymbol{y}|\big) = \frac{1}{2\pi} \int_{-\infty}^{+\infty} \frac{1}{2\gamma_q} e^{-\gamma_q|x_2-y_2|} e^{iv(x_1-y_1)} dv, \quad q = 1,2 \tag{3.20}$$

the infinite spectral integrals in (3.14) can be approximated as

$$G_p(x, y) = \frac{i}{4} \left(\sum_{n=1}^{N_p^{\{1\}}} a_{n,p} H_0^{(1)} \left(k_q \rho_{n,p}^{\{1\}} \right) + \sum_{n=1}^{N_p^{\{2\}}} c_{n,p} H_0^{(1)} \left(k_q \rho_{n,p}^{\{2\}} \right) \right) \qquad \textbf{(3.21)}$$

where

$$\rho_{n,p}^{\{1\}} = \begin{cases} \sqrt{(x_1 - y_1)^2 + \left(|x_2 + y_2| - ib_{n,p} \right)^2}, & p = 1,4 \\[2em] \sqrt{(x_1 - y_1)^2 + \left(|y_2| - ib_{n,p} \right)^2}, & p = 2,3 \end{cases}$$

$$\rho_{n,p}^{\{2\}} = \begin{cases} \sqrt{(x_1 - y_1)^2 + \left(|x_2 + y_2| - id_{n,p} \right)^2}, & p = 1,4 \\[2em] \sqrt{(x_1 - y_1)^2 + \left(|y_2| - id_{n,p} \right)^2}, & p = 2,3 \end{cases}$$

$$\textbf{(3.22)}$$

provided $q = 1$ for $p = 1,2$ and $q = 2$ for $p = 3,4$.

It should be noted that, since the terms Ψ_1 and Ψ_4, which are related to the reflected parts of Green's functions, are independent of spatial coordinates, they can be approximated only once and corresponding closed form expressions of G_1 and G_4 can be used for any pair of source and observation points. On the other hand, the transmitted terms Ψ_2 and Ψ_3 are needed to be approximated for each discrete value of x_2. Therefore, the computational efficiency of applying the DCIM for the calculation of G_1 and G_4 is considerably high compared to G_2 and G_3.

With the implementation of the two-level approach, the approximation becomes much faster since the number of samples and exponentials are dramatically reduced. Besides, an intense investigation of the function behavior to decide on the approximation parameters is not required, hence the approximation is more robust [31]. To demonstrate the performance of the two-level DCIM approach, a two-layered media where the upper half-space $x_2 > 0$ is air and the lower half-space $x_2 < 0$ is dry soil with constitutive parameters $\varepsilon_{r,soil} = 3.6$ and $\sigma_{soil} = 10^{-5}$ S/m at 300 MHz is considered.
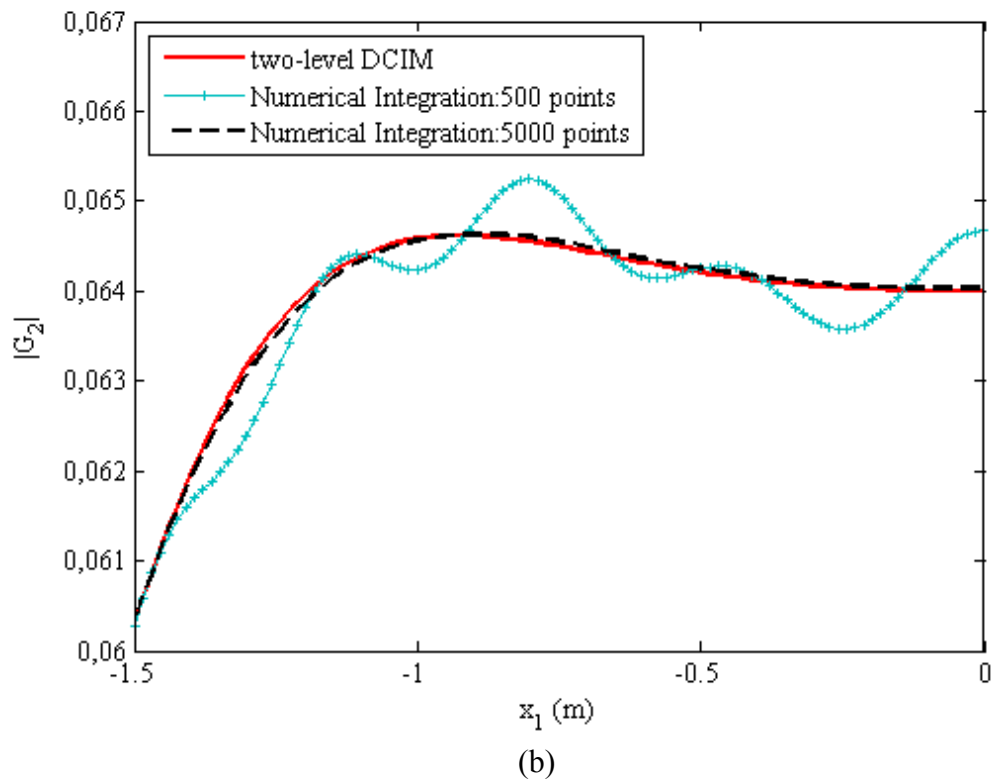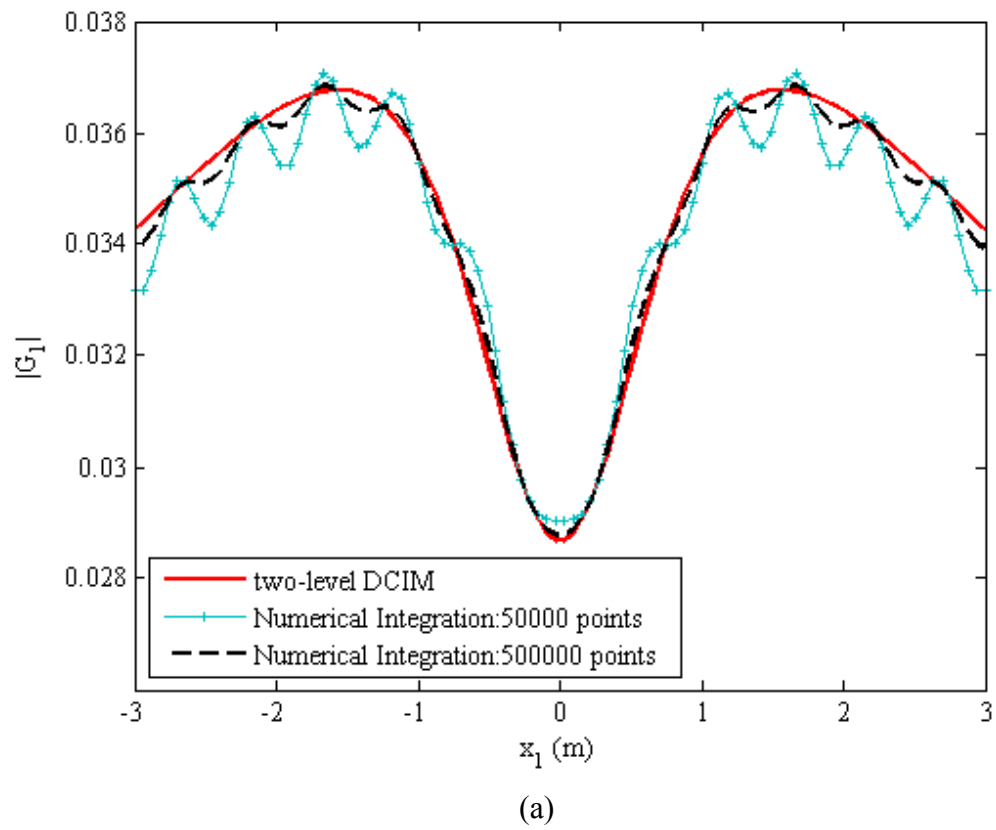
(a)

(b)

Figure 3.4: Magnitude of (a) G_1 and (b) G_2 obtained via numerical integration and the two-level DCIM at 300 MHz.

First, the variation of G_1 on a measurement line 0.3 m above the interface is calculated at 100 equidistant points due to a line source located at (0,0.4) m by using both the DCIM and the direct numerical integration through trapezoidal rule. It has been observed that, with the increasing number of samples, the numerical integration approaches the DCIM. Figure 3.4(a) demonstrates the magnitude of G_1 obtained by numerical integration with 5×10^4 and 5×10^5 sampling points and the two-level DCIM with 200 sampling points for which the resulting exponential numbers are $N_p^{\{1\}} = 5$ and $N_p^{\{2\}} = 10$. As seen in the figure, the magnitude obtained by the numerical integration with 5×10^5 sampling points barely converges to the one obtained by the two-level DCIM with 15 exponentials. The DCIM is tested also for the transmitted term G_2 by considering the same medium, and the field values due to a line source located at (0,0.04) m are computed at 100 equidistant points on the line segment defined by $-1.5 \leq x_2 \leq 0$ and $y_2 = -1.3$ which is the lower boundary of the rectangular reconstruction domain in the vast majority of the numerical applications given in Section 5. The number of sampling points required for the numerical integration in this case is much less than it is in the computation of G_1 as seen in Figure 3.4(b). However, the two-level DCIM is still more effective, since the numerical integration converges to the values obtained by the DCIM with 5000 sampling points. These results clearly indicate the strength of the two-level DCIM approach while the degree of benefit may vary according to the behaviour of the integrand for given frequency and material properties.

4. SOLUTION OF THE INVERSE SCATTERING PROBLEM

4.1 Properties of the Inverse Scattering Problem

In mathematical physics, a problem is defined as *well-posed* if it satisfies three postulates proposed by Hadamard: a solution should exist, the solution should be unique, and the solution should depend continuously on the data [39]. If a problem fails to satisfy any of these three requirements, then it is called *ill-posed*. It is shown in [30] that the direct obstacle scattering problem given by (2.10) and (2.11) is well-posed which ensures that for a known object, the scattered field is unique and continuously dependent on the constitutive parameters of the object. On the other hand,for the inverse problem in which the material properties of an unknown object are desired to be reconstructed through some scattered field data, the uniqueness of the solution is a subject of ongoing research. In $\mathbb{R}^3$ and for plane wave incidence, it is known that, if u_s is measured exactly on S for every incident direction then there is only one $\chi(\boldsymbol{x})$ that will give rise to these u_s; that is there is a unique solution of the inverse problem [30]. No results are available if u_s is known on S for only a finite number of incidence directions. Moreover, the uniqueness property has not been established even if u_s is known for all incidence directions in $\mathbb{R}^2$ [40]. In practice, both illuminations and measurementsare performed on finite number of discrete points. Then, the integral equation governing the scattering procedure will turn into an *ill-conditioned* matrix equation in which small errors in the data cause large errors in the solution. Since the measurement data contain also unavoidable noises, solution of the data equation for the source term defining the object requires regularization [30] and even in that case may not be the appropriate physical solution [40].

On the other hand, even the data equation is linear with respect to the product of the two unknowns, χu, it is highly nonlinear with respect to the contrast function χ whose reconstruction is the main purpose of the inverse problem. This nonlinearity is due to the fact that u itself is dependent on χ. This may be seen by writing the formal inverse of (2.12) as

$$u_j = (I - G^D \chi)^{-1} u_{b,j} \qquad\qquad (4.1)$$

where I denotes the identity operator. Substituting it into the data equation (2.13) yields

$$u_{S,j} = G^S \left[\chi (I - G^D \chi)^{-1} u_{b,j} \right], \qquad\qquad (4.2)$$

wherein the nonlinearity is clearly exposed. On the other hand, if $\| G^D \chi \| < 1$, the inverse operator $(I - G^D \chi)^{-1}$ can be expanded into a Neumann series as

$$(I - G^D \chi)^{-1} = \sum_{n=0}^{\infty} (G^D \chi)^n \qquad\qquad (4.3)$$

In practice, the norm $\| G^D \chi \|$ is not known, but it will depend on the geometrical dimensions of the scatterer, the frequency ω and the contrast χ [40]. In [42] the term *degree of nonlinearity* is suggested for $\| G^D \chi \|$ since it can be argued that the nonlinearity of the relationship between the unknown of the inverse problem, i.e the contrast χ, and the scattered field $u_{S,j}$ is ruled by this norm. If $\| G^D \chi \| \ll 1$, one can approximate the inverse operator as $(I - G^D \chi)^{-1} \approx I$ by truncating (4.3) at $n = 0$ and write $u_j = u_{b,j}$ in D, which is the well-known first Born approximation. Note that, through this approximation the data equation (4.2) is linearised with respect to χ. However, this is valid only for weak scatterers which have constitutive parameters close to the ones of the background or very small in size [40]. For a wide range of scatterers, the nonlinearity of the problem with respect to χ should be taken into account without applying a linearization during the solution procedure. In the literature, this has been done by recasting the inverse problem as an optimization problem of iteratively finding χ to minimise the error in the data of (2.13), subject to the constraint that the object equation (2.12) is satisfied in some sense. One can find a detailed review of such nonlinear inversion techniques in [40]. However, most of these techniques require solution of the forward problem at each step of the iterations. Hence, in this study, the Contrast Source Inversion method which is based on minimization of a cost functional that consists of errors of both the data and the object equations without solving the forward problem is applied as given below.

4.2 Solution of the Inverse Scattering Problem via the CSI

Since the contrast and the field inside the reconstruction domain occur as a product, many workers have introduced the quantity $w = \chi u$ which is called a contrast source since u_j satisfies the inhomogeneous Helmholtz equation

$$\Delta u_j(x) + k_b{}^2(x)u_j(x) = -k_b{}^2(x)w_j(x). \tag{4.4}$$

Then, the system of integral equations(2.12) and (2.13) can be rewritten for the contrast source as

$$u_j = u_{b,j} + G^D w_j, \quad j = 1, 2, \dots, J, \tag{4.5}$$

$$u_{s,j} = G^S w_j, \quad j = 1, 2, \dots, J. \tag{4.6}$$

The CSI depicts the inverse problem as a minimization problem in which one seeks the contrast sources as well as the contrast function to minimize a cost functional that consists of two terms: Sums of the residual norms in both the object equation(4.5)and the data equation (4.6)for each illumination. The explicit expression of this cost functional for the given formulation of the problem is

$$F = \frac{\sum_j \left\| u_{s,j} - G^S w_j \right\|_S^2}{\sum_j \left\| u_{s,j} \right\|_S^2} + \frac{\sum_j \left\| \chi u_{b,j} - w_j + \chi G^D w_j \right\|_D^2}{\sum_j \left\| \chi u_{b,j} \right\|_D^2} \tag{4.7}$$

where $\|.\|_S$ and $\|.\|_D$ denote the norms on $L^2(S)$ and $L^2(D)$ respectively. These norms are defined as

$$\left\| u_j \right\|_{D,S} = \langle u_j, u_j \rangle_{D,S}^{1/2} \tag{4.8}$$

with the inner product

$$\langle u_j, v_j \rangle_{D,S} = \iint_{D,S} u_j(x) \bar{v}_j(x) dx \tag{4.9}$$

23

where the overbar denotes complex conjugate. The normalization in (4.7) is chosen so that both terms are equal to one if $w_j = 0$. According to the CSI method [33], contrast sources w_j^n are constructed by the Conjugate Gradient (CG) method [41] such that the contrast sources minimize the whole cost functional for the nth iteration. Then, the object function χ^n corresponding to the nth iteration is determined to minimize the second part of the cost functional using the updated value of w_j. The process is stopped when the difference between the cost functionals of two consecutive iterations is smaller than a predetermined value. The details of the iterative process is as follows:

The data and object errors are defined as

$$\rho_j^n = u_{s,j}{}^n - G^S w_j{}^n \tag{4.10}$$

$$\varphi_j{}^n = \chi^n u_j{}^n - w_j{}^n \tag{4.11}$$

respectively, where

$$u_j{}^n = u_{b,j} + G^D w_j{}^n. \tag{4.12}$$

When $w_j{}^{n-1}$ and χ^{n-1} are known, w_j is updated as

$$w_j{}^n = w_j{}^{n-1} + \alpha_j{}^n d_j{}^n. \tag{4.13}$$

where the step size $\alpha_j{}^n$ is constant and the update directions $d_j{}^n$ are functions of position. The update directions are chosen as Polak-Ribière conjugate gradient directions [41]

$$d_j{}^0 = 0 \tag{4.14}$$

$$d_j{}^n = g_j{}^n + \frac{\langle g_j^n, g_j^n - g_j^{n-1} \rangle_D}{\langle g_j^{n-1}, g_j^{n-1} \rangle_D} d_j{}^{n-1} \qquad n \geq 1 \tag{4.15}$$

where $g_j{}^n$ is the gradient (Frechet derivative) of the cost functional with respect to w_j evaluated at $w_j{}^{n-1}$, χ^{n-1}. Explicitly this is found to be

$$g_j{}^n = -\frac{G^{S*}\rho_j^{n-1}}{\sum_k \|u_{s,k}\|_S^2} - \frac{\varphi_j^{n-1} - G^{D*}(\bar{\chi}^{n-1}\varphi_j^{n-1})}{\sum_k \|\chi_k{}^{n-1}u_{b,k}\|_D^2} \tag{4.16}$$

where G^{S*} and G^{D*} are the adjoints of G^S and G^D mapping $L^2(S)$ into $L^2(D)$ and $L^2(D)$ into $L^2(D)$, respectively. These adjoint operators are defined through the relations

$$\langle v_j, G^D \psi_j \rangle_D = \langle G^{D*} v_j, \psi_j \rangle_D, \tag{4.17}$$

$$\langle v_j, G^S \psi_j \rangle_S = \langle G^{S*} v_j, \psi_j \rangle_D. \tag{4.18}$$

Substituting (2.14) into the left-hand sides of (4.17) and (4.18) and interchanging integrations, it follows that

$$G^{D*} v_j = \iint_D \bar{G}_b(\boldsymbol{y};\boldsymbol{x}) v_j(\boldsymbol{y}) d\boldsymbol{y}, \quad \boldsymbol{x} \in D, \tag{4.19}$$

and

$$G^{S*} v_j = \iint_S \bar{G}_b(\boldsymbol{y};\boldsymbol{x}) v_j(\boldsymbol{y}) d\boldsymbol{y}, \quad \boldsymbol{x} \in D. \tag{4.20}$$

After the update directions $d_j{}^n$ are determined, the step size $\alpha_j{}^n$ is chosen so as to minimize $F(w_j{}^{n-1} + \alpha_j{}^n d_j{}^n)$ which can explicity be written as

$$
\begin{aligned}
F &= \frac{\sum_j \|u_{s,j} - G^S w_j^n\|_S^2}{\sum_j \|u_{s,j}\|_S^2} + \frac{\sum_j \|\chi^{n-1} u_j^n - w_j^n\|_D^2}{\sum_j \|\chi^{n-1} u_{b,j}\|_D^2} \\
&= \frac{\sum_j \|\rho_j^{n-1} - \alpha_j{}^n G^S d_j{}^n\|_S^2}{\sum_j \|u_{s,j}\|_S^2} + \frac{\sum_j \|\varphi_j^{n-1} - \alpha_j{}^n (d_j{}^n - \chi^{n-1} G^D d_j{}^n)\|_D^2}{\sum_j \|\chi^{n-1} u_{b,j}\|_D^2}.
\end{aligned}
$$

<div align="right">(4.21)</div>

While during an application of the conjugate gradient method, the step size could be determined through an iterative minimization scheme, for the above given functional, it can be analytically determined as

$$
\alpha_j{}^n = \left(\frac{\langle \rho_j^{n-1}, G^S d_j^n \rangle_S}{\sum_j \|u_{s,j}\|_S^2} + \frac{\langle \varphi_j^{n-1}, d_j{}^n - \chi^{n-1} G^D d_j{}^n \rangle_D}{\sum_j \|\chi^{n-1} u_{b,j}\|_D^2} \right)
$$
$$
\times \left(\frac{\|G^S d_j^n\|_S^2}{\sum_j \|u_{s,j}\|_S^2} + \frac{\|d_j{}^n - \chi^{n-1} G^D d_j{}^n)\|_D^2}{\sum_j \|\chi^{n-1} u_{b,j}\|_D^2} \right).
$$

$$(4.22)$$

Once $w_j{}^n$ is obtained, $u_j{}^n$, the total field inside the domain, can be updated via (4.12) and (4.13) as

$$
u_j{}^n = u_j{}^{n-1} + G^D d_j{}^n
$$

$$(4.23)$$

In the second part of an iteration step, since the first term of F is independent of χ, we seek the contrast χ_j to minimize the second term of the cost functional which is explicitly

$$
F_D = \frac{\sum_j \|\chi u_j^n - w_j^n\|_D^2}{\sum_j \|\chi u_j^n\|_D^2},
$$

$$(4.24)$$

for the determined values of $w_j{}^n$ and $u_j{}^n$. On the other hand, in [33], it is suggested to minimize the simpler functional

$$
F_D' = \sum_j \|\chi u_j^n - w_j^n\|_D^2
$$

$$(4.25)$$

instead of more complicated (4.24). It is observed that, this simplification retains the error reducing nature of the processfor the numerical examples treated in this study and allows easy implementation of some *a priori* information or constraints on χ_j. Equation (4.25) can be rewritten as

$$F_D' = \sum_j \iint_D \left\{ \left[\frac{\mathrm{Re}(w_j^n \bar{u}_j^n)}{|u_j^n|} - \chi^r |u_j^n| \right]^2 + \left[\frac{\mathrm{Im}(w_j^n \bar{u}_j^n)}{|u_j^n|} - \chi^i |u_j^n| \right]^2 \right\} \mathrm{d}\boldsymbol{y}$$

$$= \iint_D \left\{ \left[\chi^r (\sum_j |u_j^n|^2)^{\frac{1}{2}} - \frac{\sum_j \mathrm{Re}(w_j^n \bar{u}_j^n)}{(\sum_j |u_j^n|^2)^{1/2}} \right]^2 \right.$$

$$\left. + \left[\chi^i (\sum_j |u_j^n|^2)^{\frac{1}{2}} - \frac{\sum_j \mathrm{Im}(w_j^n \bar{u}_j^n)}{(\sum_j |u_j^n|^2)^{1/2}} \right]^2 + \sum_j \left(\frac{\mathrm{Re}(w_j^n \bar{u}_j^n)}{|u_j^n|} \right)^2 \right.$$

$$\left. - \frac{[\sum_j \mathrm{Re}(w_j^n \bar{u}_j^n)]^2}{\sum_j |u_j^n|^2} + \sum_j \left(\frac{\mathrm{Im}(w_j^n \bar{u}_j^n)}{|u_j^n|} \right)^2 - \frac{[\sum_j \mathrm{Im}(w_j^n \bar{u}_j^n)]^2}{\sum_j |u_j^n|^2} \right\} \mathrm{d}\boldsymbol{y}.$$

(4.26)

In the absence of any *a priori* information on χ, it is clear that F_D' is minimized by choosing

$$\chi^{r,n} = \frac{\sum_j \mathrm{Re}(w_j^n \bar{u}_j^n)}{\sum_j |u_j^n|^2} \qquad \chi^{i,n} = \frac{\sum_j \mathrm{Im}(w_j^n \bar{u}_j^n)}{\sum_j |u_j^n|^2}.$$

(4.27)

However, if we have *a priori* information that χ^r and χ^i are positive, then we may use this information and rewrite (4.26) as

$$F_D' = \iint_D \left\{ \chi^r \left(\left[(\chi^r \sum_j |u_j^n|^2)^{\frac{1}{2}} - \left(\frac{1}{\chi^r} \sum_j \left(\frac{\mathrm{Re}(w_j^n \bar{u}_j^n)}{|u_j^n|} \right)^2 \right)^{\frac{1}{2}} \right]^2 \right.\right.$$

$$\left. + 2(\sum_j |u_j^n|^2)^{\frac{1}{2}} \left[\sum_j \left(\frac{\mathrm{Re}(w_j^n \bar{u}_j^n)}{|u_j^n|} \right)^2 \right]^{\frac{1}{2}} - 2\sum_j \mathrm{Re}(w_j^n \bar{u}_j^n) \right)$$

$$+ \chi^i \left(\left[(\chi^i \sum_j |u_j^n|^2)^{\frac{1}{2}} - \left(\frac{1}{\chi^i} \sum_j \left(\frac{\mathrm{Im}(w_j^n \bar{u}_j^n)}{|u_j^n|} \right)^2 \right)^{\frac{1}{2}} \right]^2 \right.$$

$$\left.\left. + 2(\sum_j |u_j^n|^2)^{\frac{1}{2}} \left[\sum_j \left(\frac{\mathrm{Re}(w_j^n \bar{u}_j^n)}{|u_j^n|} \right)^2 \right]^{\frac{1}{2}} - 2\sum_j \mathrm{Re}(w_j^n \bar{u}_j^n) \right) \right\} \mathrm{d}\boldsymbol{y}.$$

(4.28)

One might consider minimizing F_D' by choosing χ^r and χ^i to be zero; however, $\chi \neq 0$ whenever $w_j \neq 0$. Hence, in [33] χ^r and χ^i are chosen so as to minimize the factors multiplying χ^r and χ^i. Since the Schwarz inequality ensures that

$$(\textstyle\sum_j |u_j^n|^2)^{\frac{1}{2}} \left[\sum_j \left(\frac{\mathrm{Re}(w_j^n \bar{u}_j^n)}{|u_j^n|} \right)^2 \right]^{\frac{1}{2}} - \sum_j \mathrm{Re}(w_j^n \bar{u}_j^n) \geq 0 \qquad \textbf{(4.29)}$$

and

$$(\textstyle\sum_j |u_j^n|^2)^{\frac{1}{2}} \left[\sum_j \left(\frac{\mathrm{Im}(w_j^n \bar{u}_j^n)}{|u_j^n|} \right)^2 \right]^{\frac{1}{2}} - \sum_j \mathrm{Im}(w_j^n \bar{u}_j^n) \geq 0 \qquad \textbf{(4.30)}$$

the factors multiplying χ^r and χ^i are minimized by choosing

$$\chi^{r,n} = \left\{ \frac{\sum_j \left(\mathrm{Re}(w_j^n \bar{u}_j^n)/|u_j^n| \right)^2}{\sum_j |u_j^n|^2} \right\}^{\frac{1}{2}} \quad \chi^{i,n} = \left\{ \frac{\sum_j \left(\mathrm{Im}(w_j^n \bar{u}_j^n)/|u_j^n| \right)^2}{\sum_j |u_j^n|^2} \right\}^{\frac{1}{2}}. \qquad \textbf{(4.31)}$$

If χ^r or χ^i is known a priori, then we can use this known value during the iterations and restrict the reconstruction procedure to the other part by using the related formula given in (4.27) or (4.31).

Finally, the starting values w_j^0 are needed to be specified. Note that the iterations can not be started with $w_j^0 = 0$ since then $\chi^{r,0} = \chi^{i,0} = 0$ and the cost functional (4.7) is undefined for $n = 1$. Therefore, the constant values

$$w_j^0 = \frac{\langle u_{s,j}, G_j^S 1 \rangle_S}{\left\| G_j^S 1 \right\|_S^2} \qquad \textbf{(4.32)}$$

that minimize the data error are chosen as the starting values for the constrast source.This completes the description of the CSI algorithm which is summarized in Table 4.1 below.

Table 4.1 :CSI in the absence of *a priori* information.

i) Determine the initial values as follows:

$$w_j{}^0 = \frac{\langle u_{s,j}, G_j^S 1 \rangle_S}{\|G_j^S 1\|_S^2}$$

$$u_j{}^0 = u_{b,j} + G^D w_j{}^0$$

$$\chi^0 = \frac{\sum_j (w_j^0 \bar{u}_j{}^0)}{\sum_j |u_j^0|^2}$$

ii) N being the maximum number of iterations, perform the following
iteration for $n = 1,2...$ N:

    1) Determine $g_j{}^n$ and then update direction $d_j{}^n$.

    2) Determine step size $\alpha_j{}^n$ that minimizes F along $d_j{}^n$.

    3) Update the contrast source as $w_j{}^n = w_j{}^{n-1} + \alpha_j{}^n d_j{}^n$.

    4) Update the total field as $u_j{}^n = u_j{}^{n-1} + G^D d_j{}^n$.

    5) Determine the contrast as $\chi^n = \dfrac{\sum_j (w_j^n \bar{u}_j{}^n)}{\sum_j |u_j^n|^2}$

    6) Calculate F^n and $\delta_F = F^{n-1} - F^n$.

    7) If $\delta_F < \epsilon$ stop the iteration before N is reached.

5. NUMERICAL SIMULATIONS

In order to test the performance of the proposed approach, some numerical simulations are performed by using a regular PC with a CPU at 2.67 GHz and 16 GB of RAM. Throughout the simulations, unless otherwise stated, 300 MHz is chosen as the working frequency. 10 equally spaced line sources are located on a line above the rough surface and the scattered field is measured at 40 discrete points for each illumination since it has been observed that using more than 10 sources and 40 measurement points does not yield remarkably improved results for the examples given here. The scattered field data are obtained synthetically by solving the direct scattering problem for an object buried under a rough surface via the Finite Element Method (FEM). Note that, the inversion procedure is based on the formulation of the Method of Moments (MoM). Thus, the synthetic data obtained by using FEM can be considered as noisy for the inversion procedure. Nevertheless, 10% random noise is introduced to the scattered field. More precisely, a random term $\eta |u_{s,j}| e^{i2\pi r_d}$ is added to the data, where η is the noise level and r_d is a uniformly distributed random variable between 0 and 1. The corresponding signal to noise ratio is then SNR = -$20\log_{10} \eta$. The Green's function of the background is obtained by solving the direct problem given by(3.1)and (3.3)via the Method of Moments with cell size of $\lambda_{soil}/14$ $\times\lambda_{soil}/14$, where λ_{soil} is the wavelength in the soil. For the simulations given here, the corresponding number of cells on the entire roughness B varies between 183 and 7574. In the application of the imaging method, the reconstruction domain $D$is chosen as a 1.5 m × 1 m rectangle and discretized with cells of size $\lambda_D/14$ $\times\lambda_D/14$. Here, the approximate minimum wavelength λ_D is determined by considering the estimated maximum relative permittivity in domain D. Accordingly, the total number of cells in domain D changes between 1350 and 14751 for the examples given here.

At each simulation, the iterative process in the application of the CSI, is performed by choosing expression (4.32) as the initial estimate of the contrast source and unless otherwise stated, by considering the positivity constraint for the contrast. The computational time for the entire procedure, including the calculation of the Green's

31

functions, as well as the iterative process, which is stopped at 500 iterations, changes approximately between 0.5 and 45 minutes according to the operation frequency, the constitutive parameters and the size of the roughness.

For the first set of simulations, the rough surface shown in Figure 5.1 is considered, and the source and measurement points are located on lines $x_2 = 0.4$ m and $x_2 = 0.3$ m respectively. Initially, a kite-shaped object having relative permittivity $\varepsilon_{r,C} = 5$ and conductivity $\sigma_C = 0.05$ S/m is buried into a half-space composed of dry soil with constitutive parameters $\varepsilon_{r,soil} = 3.6$ and $\sigma_{soil} = 10^{-5}$ S/m at 300 MHz. The entire imaging procedure is performed approximately in 9 min. Note that, it would take days if numerical integration was applied instead of the DCIM. The original relative permittivity and conductivity profiles are shown in Figure 5.1(a) and (b), in which the reconstruction domain D is indicated with the red borders, while the corresponding inversion results in the domain D are demonstrated in Figure 5.1(c) and (d), respectively. It is observed that, the shape and location as well as the relative permittivity of the object are quite well determined whereas the conductivity is partially underestimated. Note that, the reconstruction results are given in their own color scales since giving the reconstructed and the original profiles in the same scale may not be illustrative enough for visual interpretation especially in the case that the property values are significantly underestimated.

It may seem possible to image the object with the assumption that the interface between the two half-spaces is planar. Such an approach is tested by using the data obtained above. In this case, the inverse problem is solved via the CSI assuming that the two-layered media has a planar interface. Highly inaccurate results given in Figure 5.1(e) and (f) obviously indicate that, the rough surface significantly affects the problem, and thus should certainly be taken into consideration during the inversion procedure.

In order to test the performance of the proposed approach for multiple scatterers, three objects with relative permittivities 5, 8, 10 and conductivities 0.04 S/m, 0.07 S/m, 0.1 S/m are buried into the medium described above, and imaged at 300 MHz. The original and the reconstructed relative permittivity and conductivity profiles in the domain D are shown in Figure 5.2. All three objects can be clearly distinguished in the reconstruction results even though they appear to be slightly below their actual

32

positions in the reconstructed relative permittivity profiles and their conductivities are partially underestimated as in the previous example.
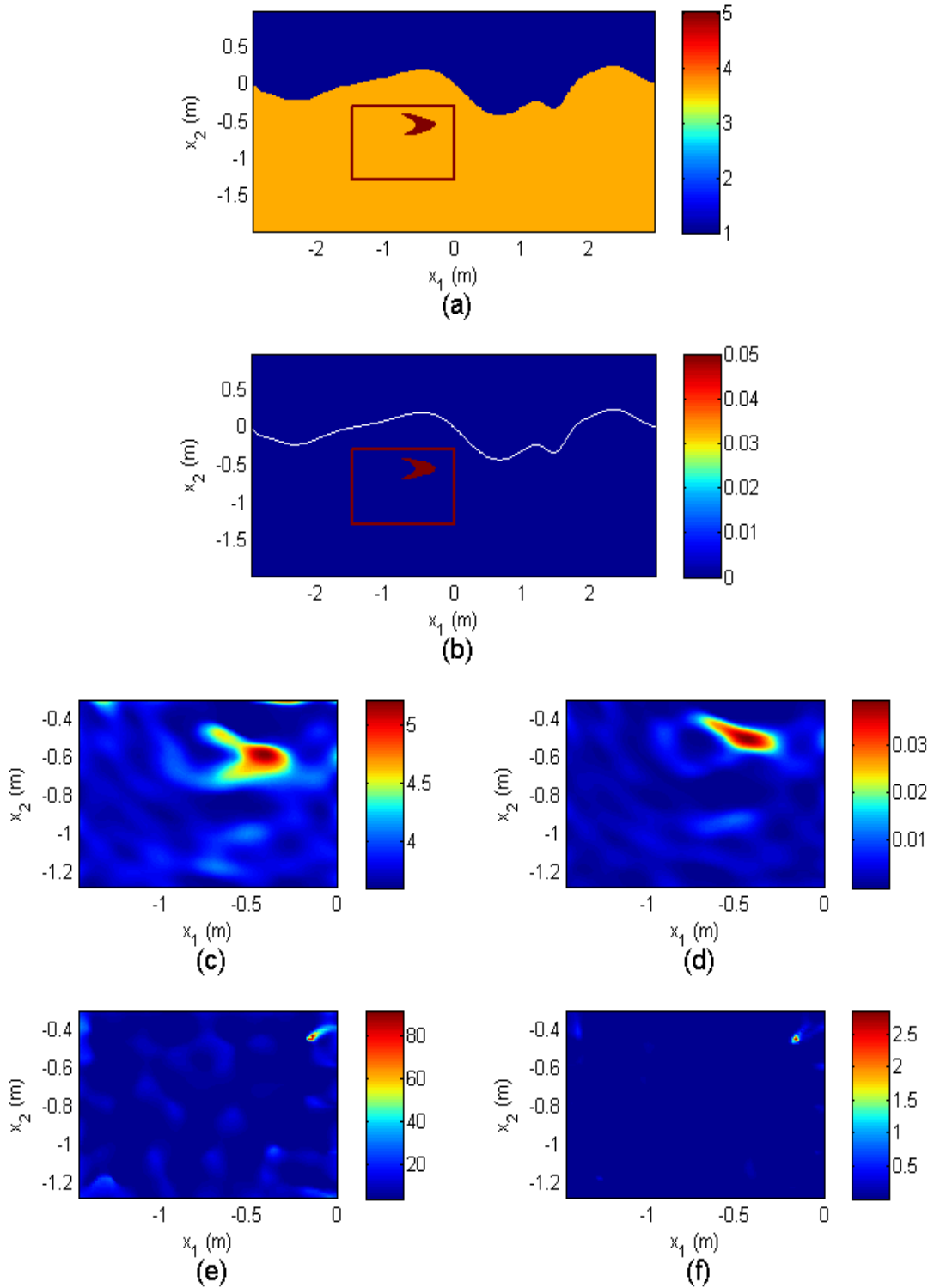

Figure 5.1: (a) The original relative permittivity and (b) conductivity profiles of the object and the background; (c) Reconstructed permittivity and (d) conductivity profiles in the domain D when the roughness is taken into consideration via the proposed approach; (e) Permittivity and (f) conductivity profiles when the interface between the half-spaces is assumed to be planar during the inversion procedure.
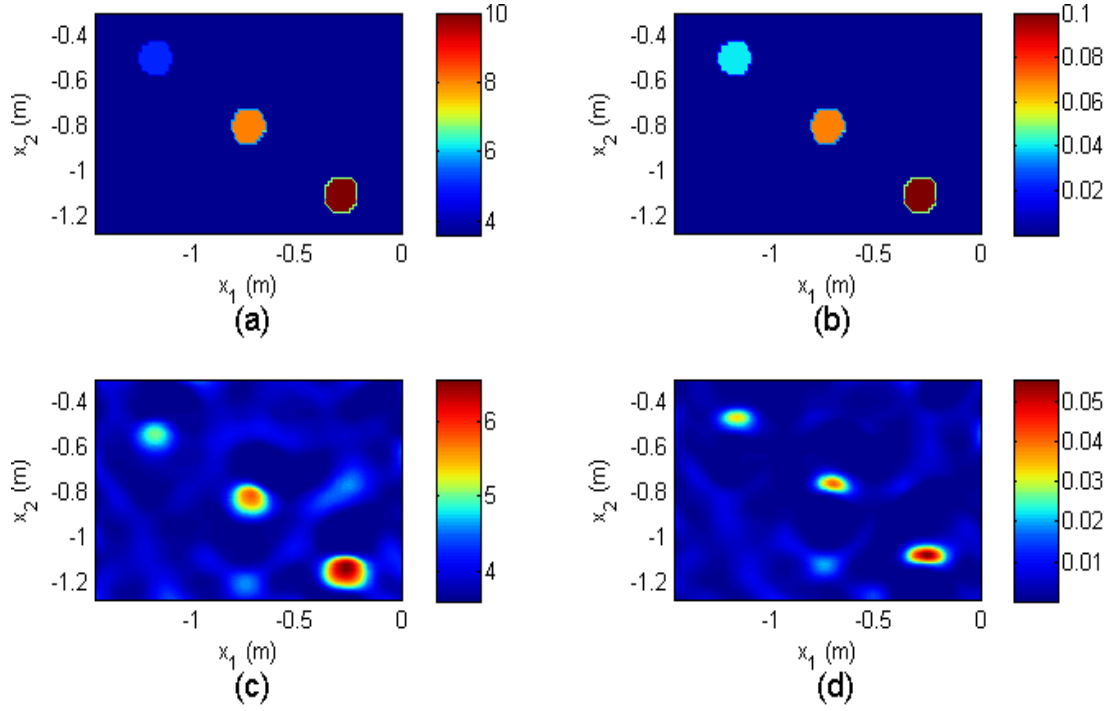
Figure 5.2: (a) The original relative permittivity and (b) conductivity profiles of multiple scatterers of different dielectric properties in the domain *D*; (c) Reconstructed relative permittivity and (d) conductivity profiles.

The kite-shaped object used in the first simulation is enlarged as shown in Figure 5.3(a) and (b) in order to investigate the effect of the object size on the performance of the imaging approach. The permittivity and conductivity profiles of the object could not be successfully reconstructed at 300 MHz as seen in Figure 5.3(c) and (d). Therefore, assuming that the constitutive parameters of both the object and the soil are unchanged, the imaging simulation is repeated at 150 MHz. As clearly seen in Figure 5.3(e) and (f), the quality of the reconstruction results is significantly improved. It is due to the fact that the *degree of nonlinearity* of the problem decreases with decreasing electrical size of the object[41]. It should also be noted that the computational time for 300 MHz is approximately same with the previous simulations while it reduces approximately to 0.5 min for 150 MHz.

To demonstrate the effect of the depth, the kite-shaped object used in the first simulation is buried about 3 m below the rough surface as shown in Figure 5.4(a) and (b). For the simulation performed at 300 MHz, inaccurate reconstruction results given in Figure 5.4(c) and (d) are obtained. As in the previous example, the imaging simulation is repeated at 150 MHz, and noticeably improved reconstruction results are achieved as seen in Figure 5.4(e) and (f). However, as might be expected, thin edges of the kite cannot be observed due to the fact that longer wavelengths reduce

the spatial resolution of any imaging procedure. Therefore, while lowering the operation frequency in order to improve the performance of the proposed approach and to decrease the computational time, one should take this issue into consideration.
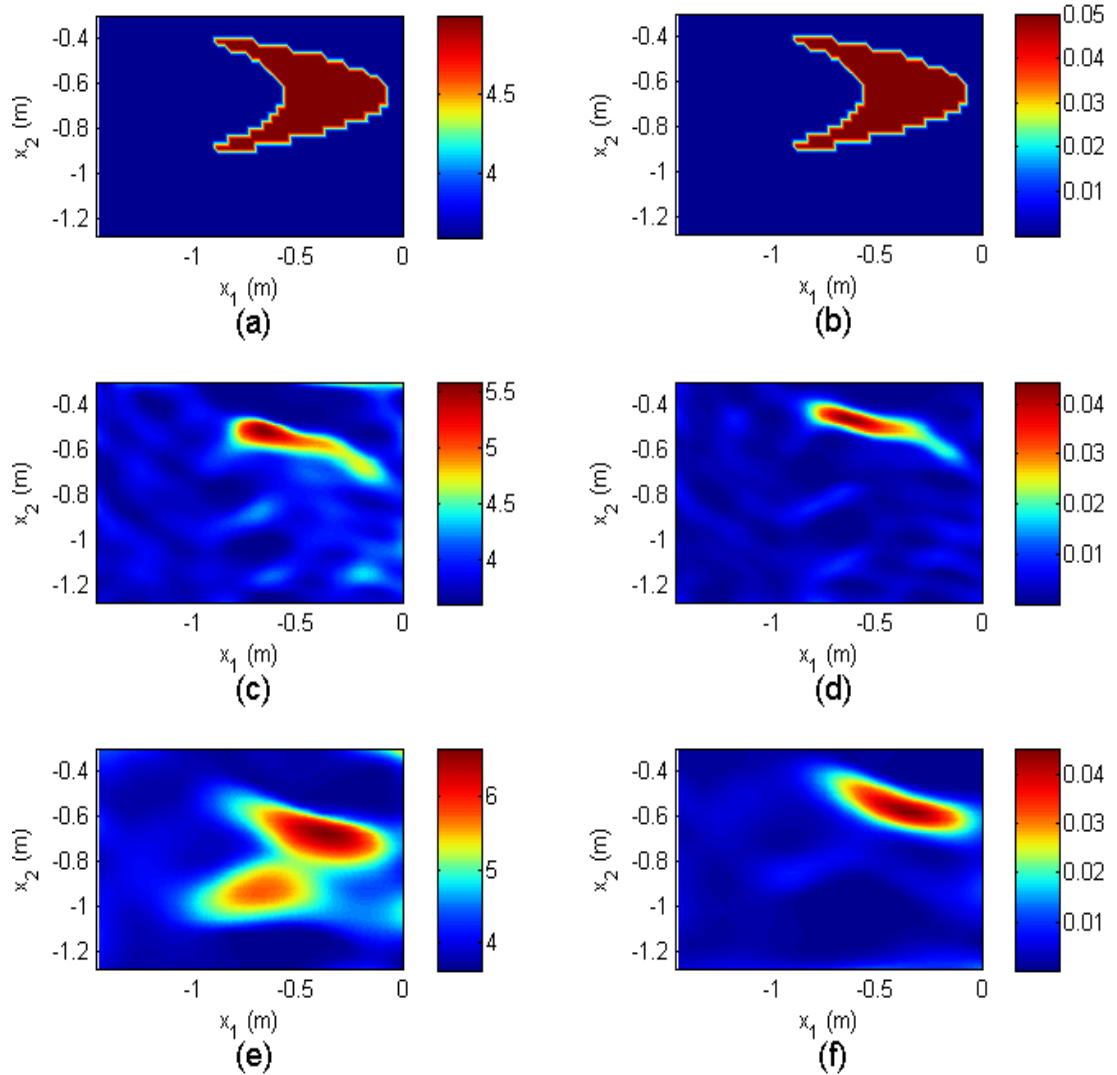

Figure 5.3: (a) The original relative permittivity and (b) conductivity profiles of a large object in the domain *D*; (c) Reconstructed permittivity and (d) conductivity profiles in the domain *D* at 300 MHz; (e) Reconstructed permittivity and (f) conductivity profiles at 150 MHz.

The reconstruction capability of the method at relatively high contrasts is tested in the same medium for a buried object whose relative permittivity is $\varepsilon_{r,c} = 40$ and conductivity is $\sigma_C = 2$ S/m as shown in Figure 5.5(a) and (b). Due to the high permittivity of the object, the number of cells in the reconstruction domain *D* increases, and accordingly the reconstruction time increases approximately to 34 min. Both the relative permittivity and conductivity of the object are significantly underestimated in the reconstruction results given in Figure 5.5 (c) and (d), but the

object can still be localized. Here, the degree of nonlinearity of the problem increases due to the high contrast between the object and the background [37].
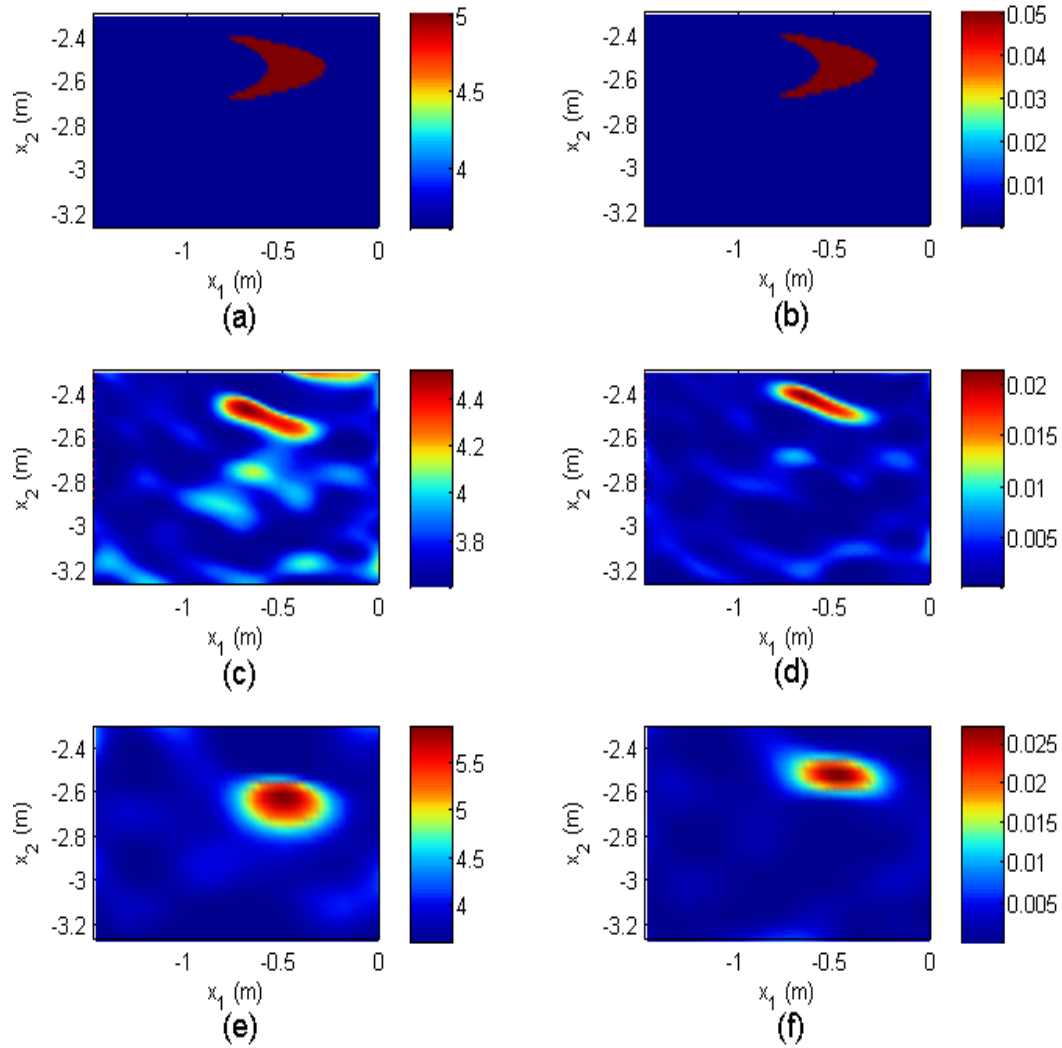

Figure 5.4: (a) The original relative permittivity and (b) conductivity profiles of the object buried in a deeper domain *D*; (c) Reconstructed permittivity and (d) conductivity profiles in the domain *D* at 300 MHz; (e) Reconstructed permittivity and (f) conductivity profiles at 150 MHz.

In order to investigate the effect of the geometry of the roughness, a rough surface with considerably larger depressions and elevations as shown in Figure 5.6is considered in the second set of simulations, and the source and measurement points are located on lines $x_2 = 1.1$ m and $x_2 = 1.0$ m, respectively. An arc-shaped object with $\varepsilon_{r,C} = 7$ and $\sigma_C = 0.1$ S/m is buried into a half-space composed of dry soil as demonstrated in Figure 5.6(a) and (b). The proposed approach sufficiently reconstructs the relative permittivity and conductivity profiles of the object in spite of the roughness size as seen in Figure 5.6(c) and (d). On the other hand, since the

number of cells used to discretize the roughness increases compared to the first example, the computational time for the entire process increases to 11 min.
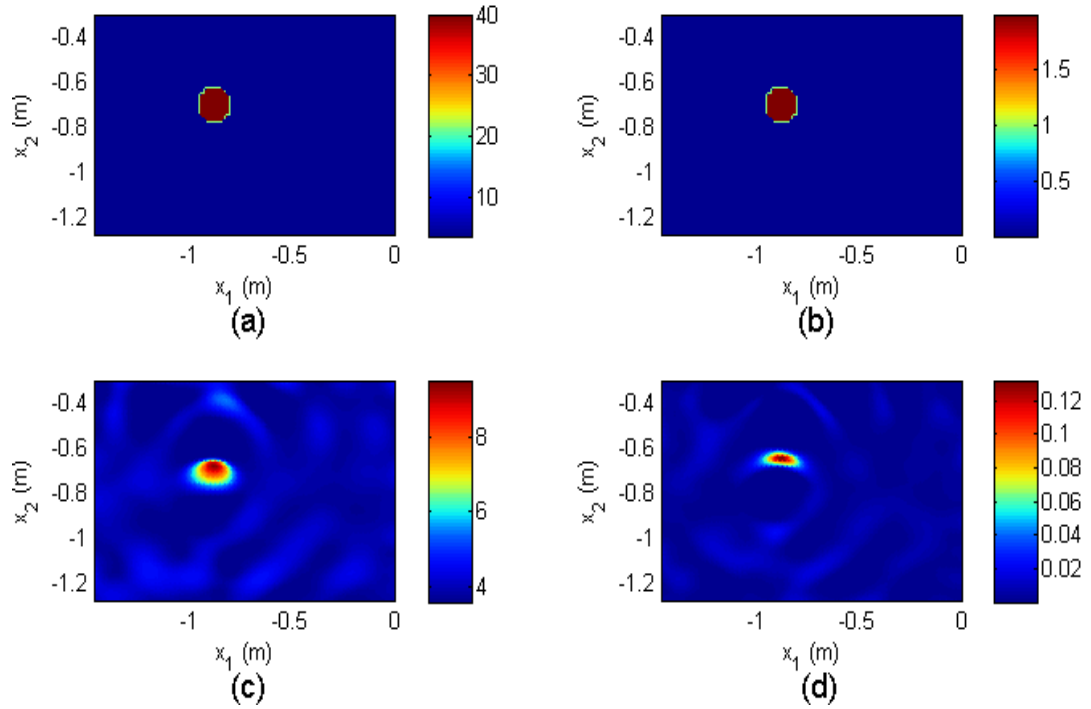

Figure 5.5: (a) The original relative permittivity and (b) conductivity profiles of an object of high contrast in the domain D; (c) Reconstructed relative permittivity and (d) conductivity profiles.

Without changing the geometry of the roughness, the lower half-space is considered to be composed of wet soil with constitutive parameters $\varepsilon_{r,soil} = 10$ and $\sigma_{soil} = 10^{-3}$ S/m, and a simulation is performed for an object with $\varepsilon_{r,C} = 25$ and $\sigma_C = 0.5$ S/m at 300 MHz. Since the number of cells used to discretize both the roughness and the domain D increases in accordance with the high constitutive parameters of the wet soil and the object, the required computational time increases to 45 min. As seen in Figure 5.7(c) and (d), increasing the constitutive parameters of the background causes a decrease in the performance of the proposed approach for this application. Improved reconstruction results given in Figure 5.7(e) and (f) are achieved when the simulation is repeated at 150 MHz approximately in 5 min. This is an expected result since it is known that higher operation frequency yields better resolution but less penetration in a lossy media.
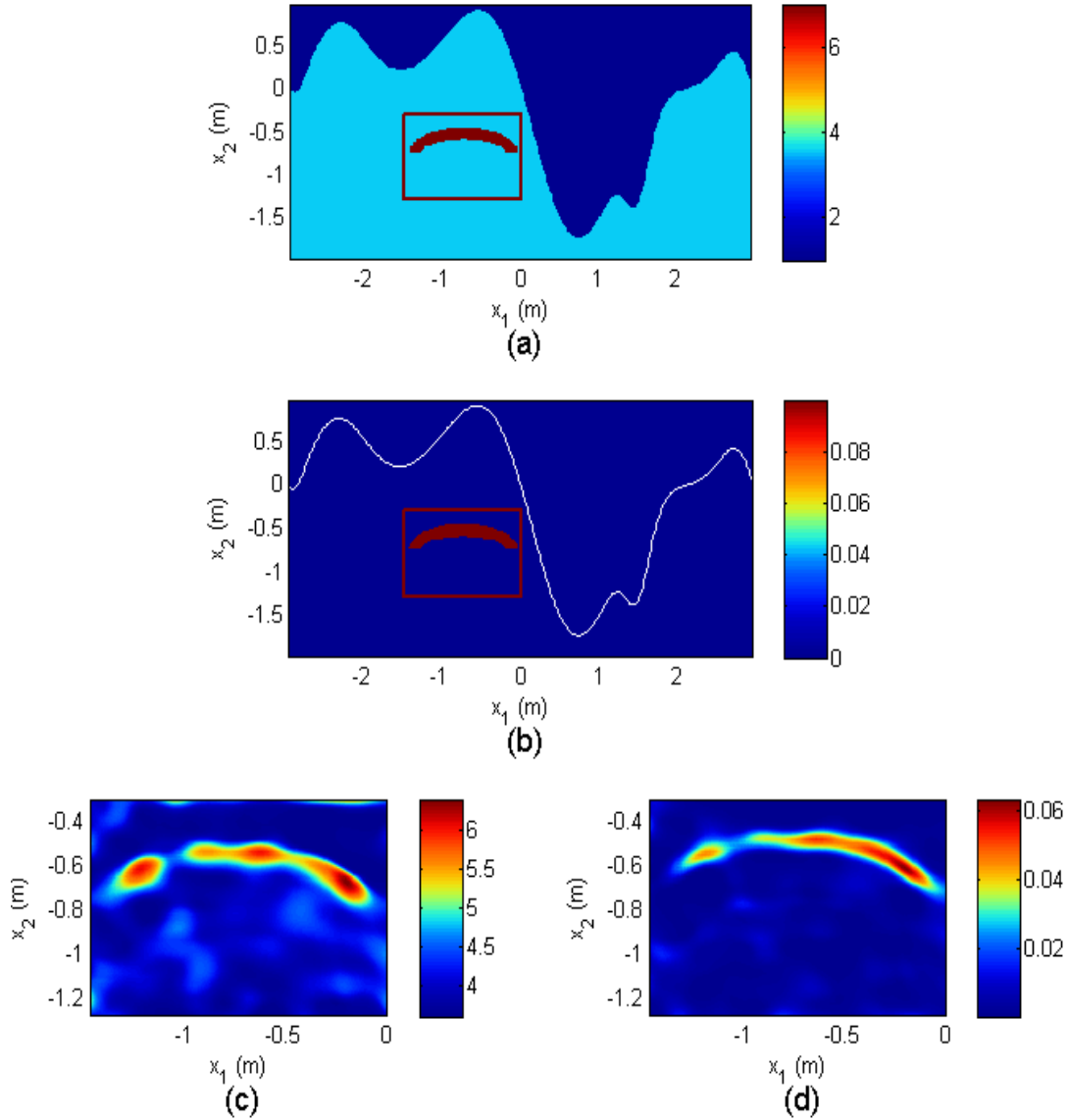
Figure 5.6: (a) The original relative permittivity and (b) conductivity profiles of the object and the background with a larger roughness; (c) Reconstructed permittivity and (d) conductivity profiles in the domain *D*.

In order to observe the performance of the method for negative contrasts, an object whose constitutive parameters are equal to those of the air, i.e. $\varepsilon_{r,B} = 1$ and $\sigma_B = 0$ S/m, is buried in the medium considered in the previous example. The iterative process in the CSI is performed without applying the positivity constraint. Although the reconstruction results are not accurate enough to determine the material properties of the object, it is still detectable especially in the reconstructed relative permittivity profile in Figure 5.8(c).
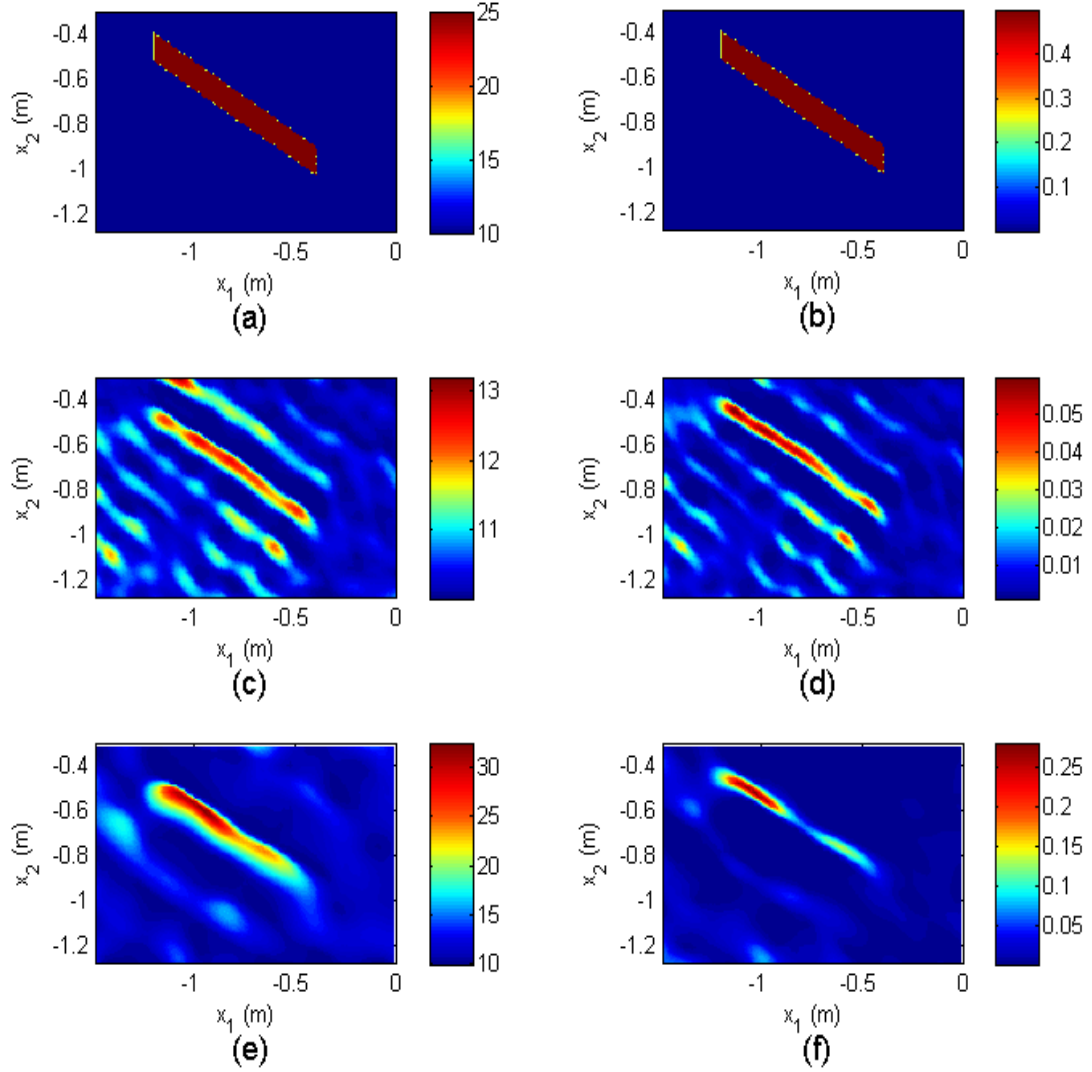
Figure 5.7: (a) The original relative permittivity and (b) conductivity profiles of an object buried in wet soil in the domain *D*; (c) Reconstructed permittivity and (d) conductivity profiles in the domain *D* at 300 MHz; (e) Reconstructed permittivity and (f) conductivity profiles at 150 MHz.

The effect of the size of the reconstruction domain *D* is investigated by enlarging the domain as shown in Figure 5.9. The domain is chosen as the region between the rough surface and the line $x_2 = 1.5$ m and the reconstruction is performed by using the data of the first example given in 6. . As clearly seen in Figure 5.9 (a) and (b), which are the real and the imaginary parts of the reconstructed contrast obtained at 300 MHz respectively, the quality of the results decreases in this case. Thus, although the object can still be detected in the contrast figures, it is almost undistinguishable in the corresponding permittivity profile given in Figure 5.9 (c). On the other hand, much better results given in Figure 5.10 are achieved at 150 MHz

while the edges of the kite-shape are lost in the reconstructions as they were in the previous examples at 150 MHz.
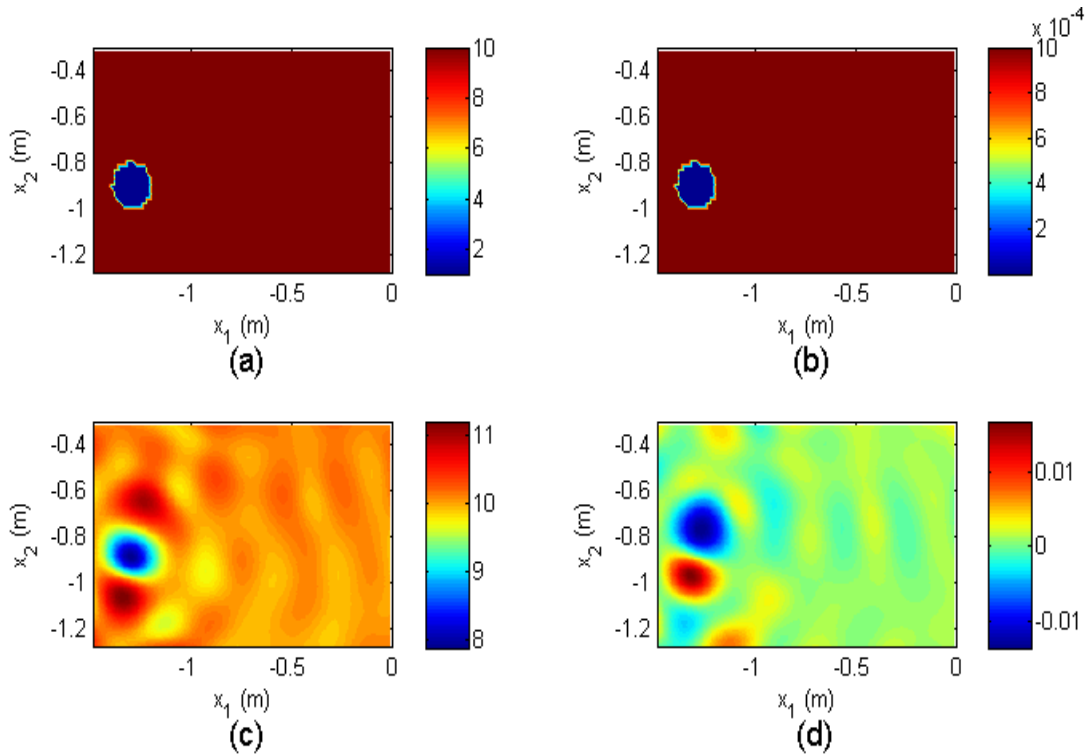

Figure 5.8: (a) The original relative permittivity and (b) conductivity profiles of an object of negative contrast in the domain *D*; (c) Reconstructed relative permittivity and (d) conductivity profiles.

Finally, a simulation is performed to test whether the method is aplicable fora more realistic case in which the lower half space is inhomogeneous. For this purpose, the dielectric parameters of soil considered in the above applications is disturbed by 15% random noise as shown in Figure 5.11(a) and (c) which are the permittivity and conductivity distributions respectively. The total field, i.e.$u(\boldsymbol{x})$ for $\boldsymbol{x} \in S$, is obtained for a kite-shaped object buried into this inhomogeneous half-space. Then the proposed approach is applied throughthe computation of the Green's function as well as of the background field for the homogeneous half space given in Figure 5.11(b) and (d) which are the assumed permittivity and conductivity profilesrespectively. For such a scenerio, the object can still be identified, despite a reduction in the quality of the results given in Figure 5.12.
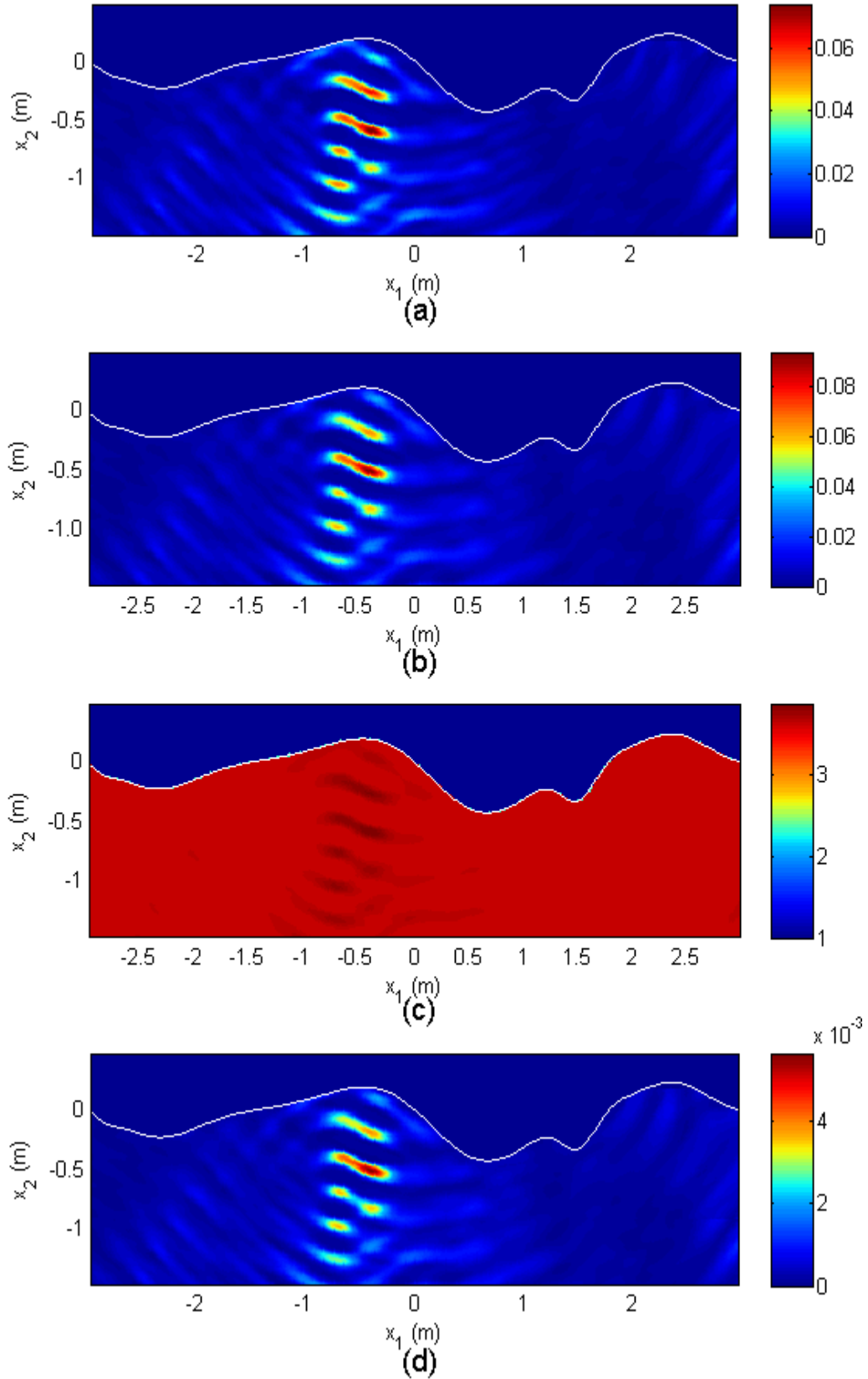
Figure 5.9 : (a) Real and (b) imaginary parts of the reconstructed contrast for a larger domain; Corresponding (c) permittivity and (d) conductivity profiles at 300 MHz.

Figure 5.10 : (a) Real and (b) imaginary parts of the reconstructed contrast for a larger domain; Corresponding (c) permittivityand (d) conductivity profiles at 150 MHz.
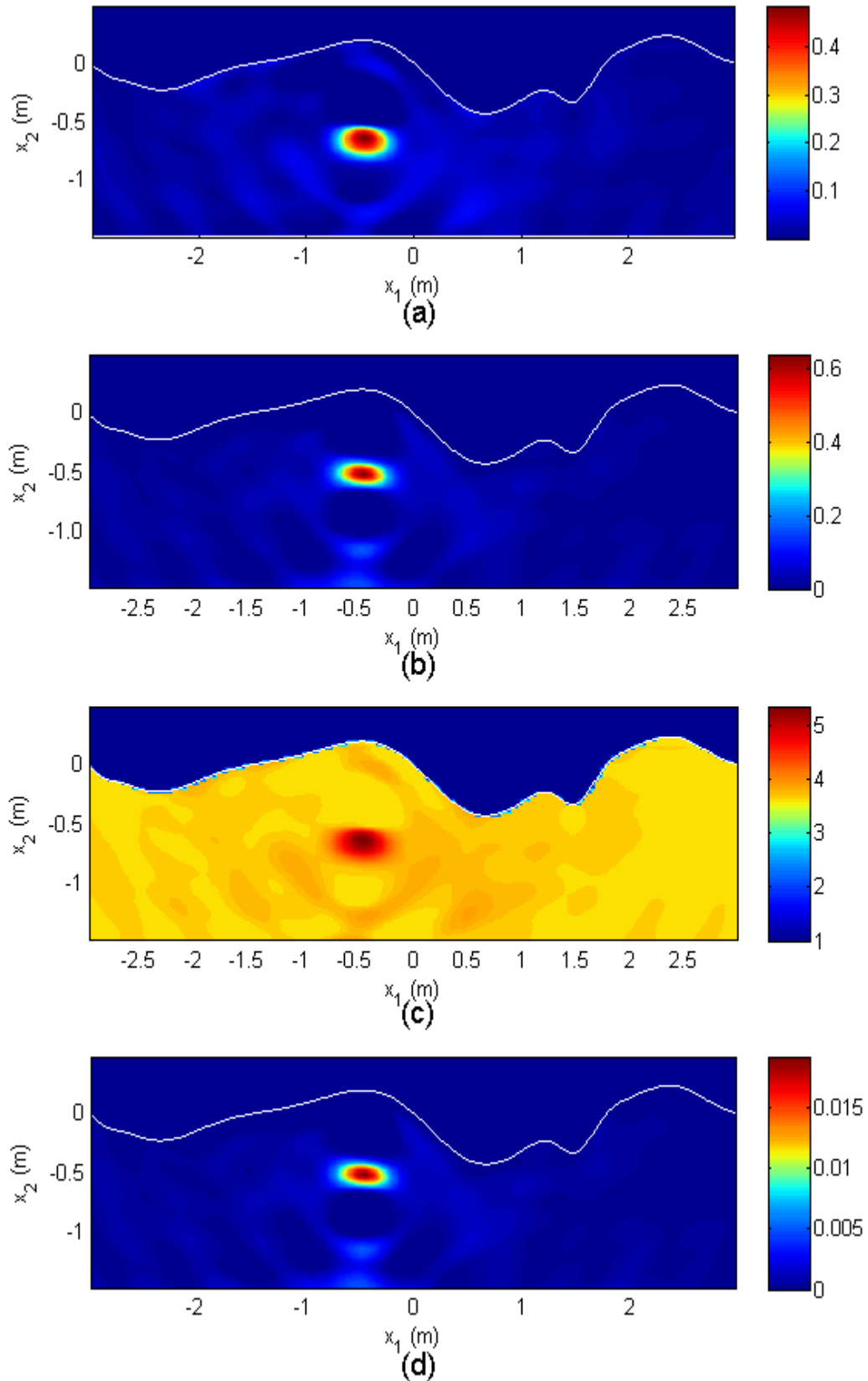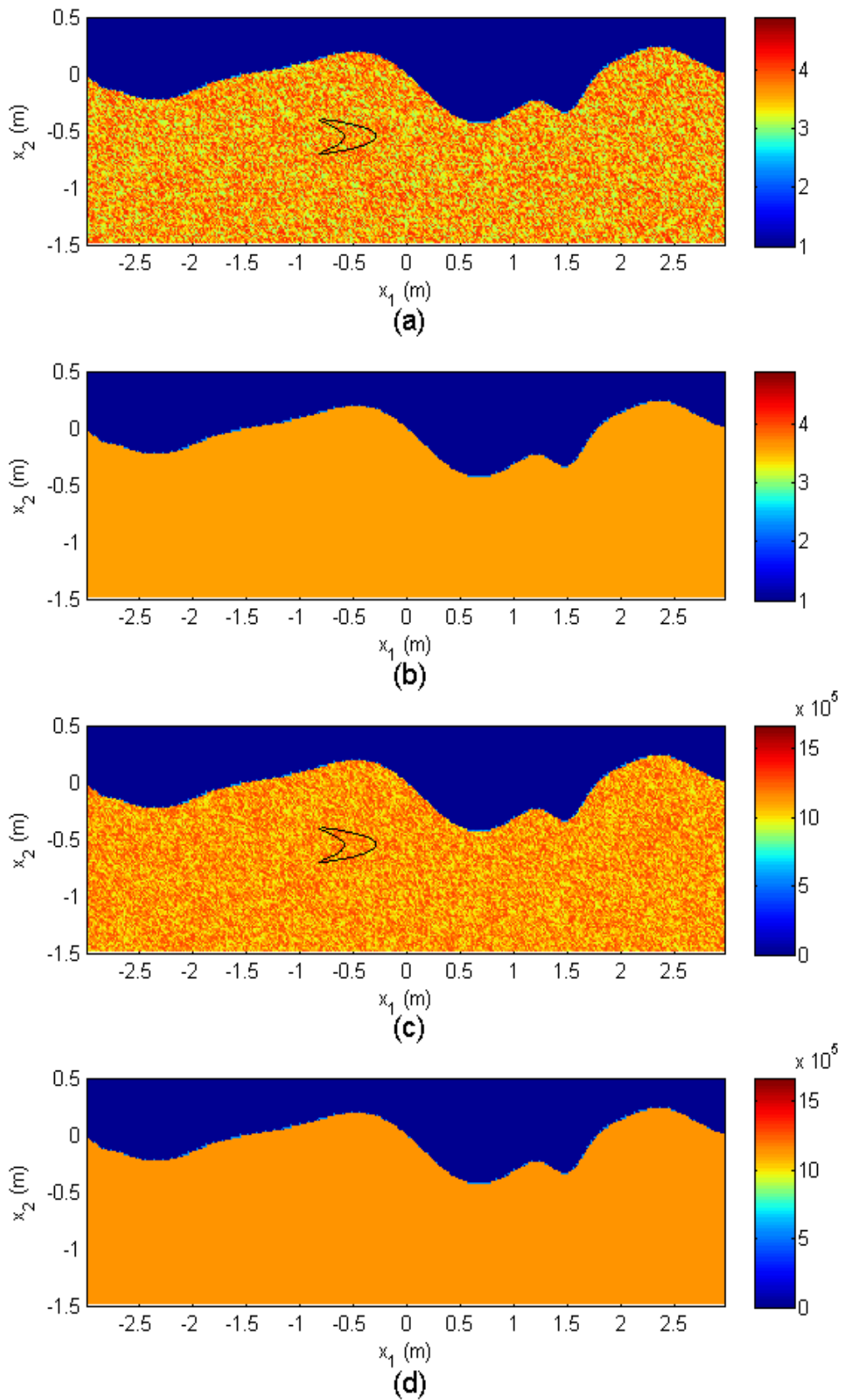
Figure 5.11 : (a) Exact and (b) assumed relative permittivity profiles for an inhomogeneous lower half-space; (c) Exact and (d) assumed conductivity profiles.

43
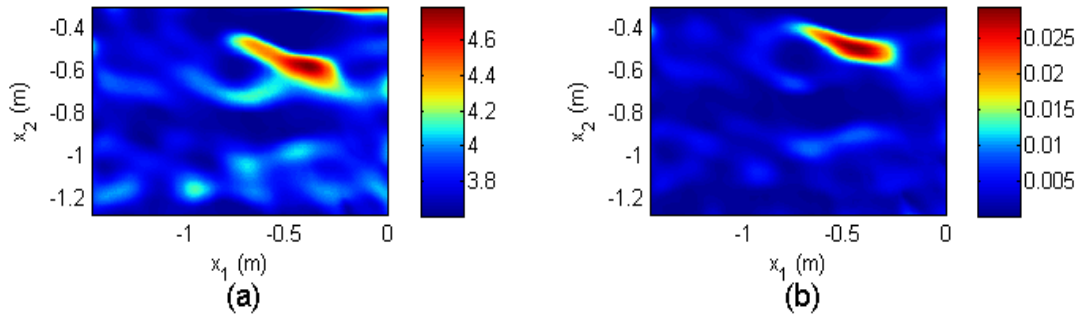
Figure 5.12 : (a) Relative permittiviy and (b) conductivity profiles in the reconstruction domain D when the inversion is performed by assuming the inhomogeneous lower half-space to be homogeneous.

In some of the above applications, objects appear to be slightly below their actual positions although their property Svalues are reconstructed in a feasible accuracy. In this case, any measure of the errors based on the pixel by pixel comparison of the profiles may yield disproportionately high values. Thus, in order not to lead to an unfair comparison of the results, it is preferred to give the exact and the reconstructed profiles for visual interpretation without giving a measure of the error.

8. CONCLUSIONS

A nonlinear tomographic approach for microwave imaging of dielectrics buried under a rough surface is presented. The contribution of the roughness to the problem is taken into consideration via the Buried Object Approach which assumes the roughness as a series of objects located alternately on both sides of the planar interface of a layered media. The Green's function of the two-layered media with a planar interface is required in such an approach, and is computed fast and accurately by the implementation of the two-level DCIM which makes the proposed approach more practicable. Finally, the resulting integral equations that govern the scattering from the buried object are solved for the contrast function by using the standard CSI method.

Through the numerical simulations with noise added data, it has been shown that the proposed approach yields good reconstructions despite the incompleteness of the data. Even multiple scatterers of relatively small size can be distinguished by their properly reconstructed constitutive parameters. Moreover, objects with higher constitutive parameters are still detected and localized although the results are far from high accuracy. Besides, we conclude from the simulations performed for various roughness geometries, two of which are given in this paper, that the geometry of the roughness does not considerably affect the quality of the reconstructions. On the other hand, it is clear that, increasing the size of the roughness in terms of the wavelength will increase the computational time, since the proposed approach requires solution of the forward problem associated with the roughness. It has been observed that lowering the operation frequency improves the performance of the method and reduces the computational time for objects relatively large in size or buried in a lossy medium such as wet soil. Such an improvement with lowered operation frequency has also been observed for objects buried deep into ground, even if the ground is nearly lossless. Nevertheless, while lowering the operation frequency, one should take the reduction in the spatial resolution of the reconstructions into consideration. Finally it is worth to note that applying the a

priori information about the positivity of the contrast enhances the performance of the method. On the other hand, in order to show that objects having negative contrast values are still detectable without applying any a priori information during the inversion procedure, an object whose constitutive parameters are equal to those of the air is buried into the ground that consists of wet soil and imaged via the proposed approach. The reconstruction results of this simulation can be interpreted that the proposed approach is not only applicable for imaging of buried dielectrics but also for determination of hollows or pipes in an inaccessible half-space.

The proposed approach can also be applied to multilayered media having more than two layers. We note that the approach given here has two main computational steps: *i*) the solution of the forward problems for $G_b(x; y)$ and $u_b(x)$, *ii*) the inversion procedure via the CSI. In the case of more than two layers, the computational time required for the CSI will not be affected since this step is related to the field values on the reconstruction and measurement domains only. On the other hand, if the lower layers have planar interfaces, the required computational time for the solution of the forward problems will not be significantly affected since just more reflection and transmission coefficients will be needed to be calculated analytically in this case. However, if the layers have rough interfaces of similar sizes, the computational time will increase approximately as a multiple of the number of interfaces.

Furthermore, there is no objection to the expansion of the method, which is considered in 2D in this paper, to 3D. Future work is focused on such an expansion and implementation of modified Contrast Source Inversion algorithms in order to improve the quality of the reconstructions especially for high contrast values.

REFERENCES

[1] **Lambert, M., Lesselier, D., and Kooij, B. J.** (1998). The retrieval of a buried cylindrical obstacle by a constrained modified gradient method in the *H*polarization case and for Maxwellian materials,*Inverse Problems*, vol. 14, no. 5, 1265-1283.

[2] **Dubois, A., Belkebir,K., and Saillard, M.** (2004). Localization and characterization of two-dimensional targets buried in a cluttered environment,*Inverse Problems*, vol. 20, no. 6,63-79.

[3] **Chaturverdi, P., and Plumb, R. G.** (1995). Electromagnetic imaging of underground targets using constrained optimization,*IEEE Transactions on Geoscience and Remote Sensing*, vol. 33, no. 3, 551-561.

[4] **Yu, Y., Yu, T., and Carin, L.** (2004). Three dimensional inverse scattering of a dielectric target embedded in a lossy half-space, *IEEE Transactions on Geoscience and Remote Sensing*, vol. 42, no. 5, 957-973.

[5] **Cui, T. J., Aydiner, A.A., Chew, W.C., Wright, D. L., and Smith, D.V.** (2003). Three-dimensional imaging of buried objects in very lossy earth by ınversion of VETEM Data, *IEEE Transactions on Antennas and Propagation*, vol. 41, no. 10, 2197-2210.

[6] **Cui, T. J.,Qin, Y., Ye, Y., Wu, J., Wang G. L., andChew, W.C.** (2006). Efficient low-frequency inversion of 3D buried objects with large contrasts,*IEEE Transactions on Geoscience and Remote Sensing*,vol. 44, no. 1, 3-9.

[7] **Vertiy, A. A., and Gavrilov, S. P.** (1998). Modeling of Microwave Images of Buried Cylindrical Objects,*International Journal of Infrared and Millimeter Waves*, vol. 19, no. 9, 1201-1220.

[8] **Li, F., Liu, Q. H., and Song, L.** (2004). Three-dimensional reconstruction of objects buried in layered media using Born and Distorted Born iterative methods,*IEEE Geoscience and Remote Sensing Letters*, vol. 1, no. 2, 107-111.

[9] **Cui, T. J., Chew, W. C., Aydiner, Chen, S.** (2001). Inverse scattering of two-dimensional dielectric objects buried in a lossy earth using the distorted Born iterative method,*IEEE Transactions on Geoscience and Remote Sensing*,vol. 39, no. 2, 339-346.

[10] **Cakoni, F., Fares, M., and Haddar, H.** (2006). Analysis of two linear sampling methods applied to electromagnetic imaging of buried objects, *Inverse Problems,* vol. 22, no. 3, 845-867.

[11] **Morrow, I.L., and Genderen, P.V.** (2002). Effective imaging of buried dielectric objects,*IEEE Transactions on Geoscience and Remote Sensing*,vol. 40, no. 4, 943-949.

[12] **Li, F., Chen, X., and Huang, K.-M.** (2008). Microwave imaging a buried object by the GA and using the s11 parameter,*Progress In Electromagnetics Research*, vol. 85, 289-302.

[13] **Chen, X., Huang K.-M., and Xu X.-B.** (2005). Microwave imaging of buried inhomogeneous objects using parallel genetic algorithm combined with FDTD method,*Progress In Electromagnetics Research*, 53, 283-298.

[14] **Caorsi,S., Massa,A., Pastorino,M., Raffetto,M., and Randazzo,A.** (2003). Detection of buried inhomogeneous elliptic cylinders by a memetic algorithm,*IEEE Transactions on Antennas and Propagation*, vol. 51, no. 10, 2878-2884, 2003.

[15] **Altuncu,Y., Akduman, I., and Yapar,A.** (2007). Detecting and Locating Dielectric Objects Buried Under a Rough Interface,*IEEE Geoscience and Remote Sensing Letters*, vol. 4, no. 2, 251-255.

[16] **El-Shenawee,M.** (2003). Remote sensing of penetrable objects buried beneath two-dimensional random rough surfaces by use of the Mueller matrix elements, *Journal of the Optical Society of America* A, 117, 183–194.

[17] **El-Shenawee,M.** (2004). Polarimetric scattering from two-layered two-dimensional random rough surfaces with and without buried objects,*IEEE Transactions on Geoscience and Remote Sensing*, vol. 42, no. 1, 67-76.

[18] **O'Neill,K.** (2000). Broadband bistatic coherent and incoherent detection of buried objects beneath randomly rough surfaces, *IEEE Transactions on Geoscience and Remote Sensing*, vol. 38, no. 2, 891-898.

[19] **Cmielewski,O., Saillard,M., and Tortel,H.** (2006). Detection of buried objects beneath a rough surface,*Waves in Random and Complex Media*, vol. 16, no. 4, 417-431.

[20] **Zhu,X., Zhao, Z., Yang, W., Zhang, Y., Nie, Z.-P., and Liu, Q. H.** (2011). Iterative time-reversal mirror method for imaging the buried object beneath rough ground surface,*Progress In Electromagnetics Research*, vol. 117, 19–33.

[21] **Wang,Y., Longstaff,I.D., and Leat,C.J.** (2001). SAR imaging of buried objects from MoM Modelled scattered field,*IEE Proceedings Radar, Sonar and Navigation*,vol. 148, no. 3, 167-172.

[22] **Ozdemir, O. and Haddar, H.** (2010). Preprocessing the reciprocity gap sampling method in buried-object imaging experiments,*IEEE Geoscience and Remote Sensing Letters*, vol. 7, no. 4, 756-760.

[23] **Cmielewski, O., Tortel, H., Litman, A., and Saillard, M.** (2007). A two-step procedure for characterizing obstacles under a rough surface from bistatic measurements,*IEEE Transactions on Geoscience and Remote Sensing*, vol. 45, no. 9, 2850-2858.

[24] **Firoozabadi, R., Miller, E.L., Rappaport, Y.C.M., and Morgenthaler, A.W.** (2007). Subsurface sensing of buried objects under a randomly rough surface using scattered electromagnetic field data,*IEEE Transactions on Geoscience and Remote Sensing*, vol. 45, no. 1, 104-117.

[25] **Altuncu, Y., Ozdemir, O., Akduman, I., and Yapar, A.** (2006). Imaging of dielectric objects buried under an arbitrary rough surface, *Proceedings of theIEEE International Geoscience and Remote Sensing Symposium,*vol. 6,2954-2957, Denver, July

[26] **Altuncu, Y., Akleman, F., Semerci, O., and Ozlem, C.** (2008). Imaging of dielectric objects buried under a rough surface via distorted born iterative method,*Journal of Physics: Conference Series,*vol. 135, no. 1, Paris, Jun.

[27] **Altuncu, Y., Yapar, A., and Akduman, I.** (2007). Numerical computation of the Green's function of a layered media with rough interfaces, *Microwave and Optical Technology Letters*, vol. 49, no. 5, 1204-1209.

[28] **Gilmore, C., Mojabi, P., and LoVetri, J.** (2009). Comparison of an Enhanced Distorted Born Iterative Method and the Multiplicative-Regularized Contrast Source Inversion method,*IEEE Transactions on Antennas and Propagation*, vol.57, no.8, 2341-2351.

[29] **Sommerfeld, A.** (1949).*Partial Differential Equations in Physics*, Academic Press, New York.

[30] **Colton, D., Kress, R.** (1998). *Inverse Acoustic and Electromagnetic Scattering Theory*, Springer, Berlin.

[31] **Aksun, M. I.** (1996). A robust approach for the derivation of closed-form Green's functions,*IEEE Transactions on Microwave Theory and Techniques*, vol. 44, no. 5, 651-658.

[32] **Aksun, M. I.,Caliskan, F., and Gurel L.** (2002). An efficient method for electromagnetic characterization of 2-D geometries in stratified media,*IEEE Transactions on Microwave Theory and Techniques*, vol. 50, no.5, 1264-1274.

[33] **Van Den Berg, P. M.,and Kleinman, R.E**. (1997). A contrast source inversion method,*Inverse Problems*, vol. 13, no. 6, 1607–1620.

[34] **Richmond, J. H.** (1965). Scattering by a dielectric cylinder of arbitrary cross section shape,*IEEE Transactions on Antennas and Propagation*, vol. 13, iss. 3, 334–341.

[35] **Boix, R. R., Fructos, A. L., and Mesa, F.** (2010). Closed-Form Uniform Asymptotic Expansions of Green's Functions in Layered Media,*IEEE Transactions on Antennas and Propagation*, vol.58, no.9, 2934-2945.

[36] **Paulus, M., Gay-Balmaz, P., and Martin, O. J. F.** (2000). Accurate and efficient computation of the Green's tensor for stratified media,*Physical Review E*, vol.62, no.4, 5797-5807.

[37] **Chow, Y. L., Yank, J. J., Fang, D. G., and Howard, G. E.** (1991).A closed-form spatial Green's function for the thick microstrip substrate,*IEEE Transactions on Microwave Theory and Techniques*, vol. 39, 588-592.

[38] **Hua,Y. andSarkar, T. K.** (1989). Generalized pencil-of-function method for extracting poles of an EM system from its transient response,*IEEE Transactions on Antennas and Propagation*,vol.37, iss. 2, 229–234.

[39] **Hackbusch, W.** (1994).*Iterative Solution of Large Sparse Systems of Equations*, Springer, New York.

[40] **Van Den Berg, P.** (2001). Nonlinear scalar inverse scattering: Algorithms and applications in *Scattering*, Eds. Pike R. and Sabatier P., Academic Press, London.

[41] **Chong, E. K. P. and Zak, S. H.** (2001). *Introduction to Optimization*, Wiley, New York.

[42] **Bucci, O., Cardace, N., Crocco, L., and Isernia, T.** (2001). Degree of nonlinearity and a new solution procedure in scalar two-dimensional inverse scattering problems,*Journal of the Optical Society of America A*,vol. 18, no. 8, 1832-1843.

CURRICULUM VITAE

Name Surname: Tolga Ulaş Gürbüz

Place and Date of Birth: Burdur,1980

E-Mail: tolgaulasg@gmail.com

B.Sc.: Electrical and Electronics Engineering, Yeditepe University

M.Sc.: Telecommunications Engineering, Istanbul Technical University

List of Publications and Patents:

- **Gürbüz, T.U.,**Aslanyürek, B., Karabulut, E.P., and Akduman, I. (2014). An Efficient Nonlinear Imaging Approach for Dielectric Objects Buried under a Rough Surface, *IEEE Transactions on Geoscience and Remote Sensing*,vol.52, iss. 7, doi: 10.1109/TGRS.2013.2268662.

- **Gürbüz, T.U.,**Aslanyürek, B., Yapar, A., Şahintürk, H., and Akduman, I., A Nonlinear Microwave Breast Cancer through Realistic Body-Breast Modeling, (under review)

- **Gürbüz, T. U.,**Aslanyürek, B., and Akduman, I. (2013). Efficient Imaging of 3D Objects Located in a Layered Media with Rough Interfaces, *Progress in Electromagnetics Research Symposium*, Stockholm, August.

- Aslanyürek, B., **Gürbüz, T. U.,**and Şahintürk, H. (2013). Shape Reconstruction of a Dielectric Coated PEC through Generalized Impedance Boundary Conditions, *Progress in Electromagnetics Research Symposium*, Stockholm, August.

- **Gürbüz, T.U.,**Aslanyürek, B., Akduman, I.,Yapar, A., and Şahintürk, H. (2011). A contrast source imaging approach for microwave breast cancer detection, *Proceedings of13th ISMOT Int. Symp. Microwave Opt. Tech*., Prague, June.

- Akduman, I., **Gürbüz**, **T.U.**, Aslanyürek, B., Güren, O., Yapar, A., Ergene, L. T., and Şahintürk, H. (2010). A novel two step procedure for microwave breast cancer imaging, *Proceedings of 6th Int. Workshop on Biological Effects of Elecctromagnetic Fields*, Bodrum, October.

PUBLICATIONS/PRESENTATIONS ON THE THESIS

- **Gürbüz, T. U.**, Aslanyürek, B., Karabulut, E. P., and Akduman, I. (2014). An Efficient Nonlinear Imaging Approach for Dielectric Objects Buried under a Rough Surface, *IEEE Transactions on Geoscience and Remote Sensing*, vol.52, iss. 7, doi: 10.1109/TGRS.2013.2268662.

- Aslanyürek, B., **Gürbüz, T. U.**, and Şahintürk, H. (2013). Shape Reconstruction of a Dielectric Coated PEC through Generalized Impedance Boundary Conditions, *Progress in Electromagnetics Research Symposium*, Stockholm, August.